Striatal neural ensemble codes for voluntary locomotor and involuntary dyskinetic movements

Gaurav Chattree[1,2*], Radosław Chrapkiewicz[2,3], Yanping Zhang[2,4], Jane Li[2,3,5], Mark J. Schnitzer[2–7*]

[1]*Dept. of Neurology & Neurological Sciences, Stanford University, Stanford CA 94305 USA*

[2]*CNC Program, Stanford University, Stanford CA 94305 USA*

[3]*James Clark Center, Stanford University, Stanford CA 94305 USA*

[4]*Howard Hughes Medical Institute, Stanford University, Stanford CA 94305 USA*

[5]*Dept. of Biology, Stanford University, Stanford CA 94305 USA*

[6]*Dept. of Applied Physics, Stanford University, Stanford CA 94305 USA*

[7]*Dept. of Neurosurgery, Stanford University, Stanford CA 94305 USA*

[*]Corresponding authors: gchatt@stanford.edu; mschnitz@stanford.edu

SUMMARY

Classical models of movement control posit that striatal spiny projection neurons of the basal ganglia's direct and indirect pathways (dSPNs and iSPNs) respectively promote and suppress movement. Supporting this view, physiological recordings have revealed imbalanced dSPN and iSPN activity levels during hypokinetic and hyperkinetic movement conditions. However, in normal brain states, dSPN and iSPN ensembles have approximately equal activation amplitudes and time courses, jointly encoding specific actions. How pathological movement conditions alter such action coding remains poorly understood. Here we imaged the concurrent dynamics of dSPNs and iSPNs in behaving mice across normal, hypokinetic, and hyperkinetic conditions, before and after administration of drug treatments used clinically. Analyses focused on resting periods and neural activity that immediately preceded movement, examining how SPNs encoded upcoming actions. In hypokinetic states, the dSPN population was hypoactive relative to the iSPN population, consistent with prior reports. Moreover, individual dSPNs and iSPNs that encoded upcoming locomotion exhibited a reduced measure of activity compared to the normal state; the extent of this reduction predicted the degree of decline in the occurrence of locomotion. Levodopa (L-DOPA) and amantadine treatments both improved locomotion frequency but acted via distinct mechanisms. L-DOPA rebalanced the

activity of the dSPN and iSPN populations, whereas amantadine boosted the activity of individual locomotion-related dSPNs and iSPNs. In hyperkinetic states modeling L-DOPA-induced dyskinesia, dSPN populations were hyperactive relative to iSPN populations. Involuntary dyskinetic movements engaged individual dSPNs and iSPNs distinct from those encoding voluntary locomotion. Amantadine treatment reduced the resting activity of dyskinesia- but not locomotion-related SPNs without improving the overall dSPN and iSPN imbalance. These findings highlight the importance of SPN action coding, not merely the extent of activity balance, for normal and pathological movements. The results delineate two distinct therapeutic mechanisms, one that rebalances the activity of the direct and indirect pathways and another that selectively potentiates or depresses the activity of SPN populations encoding voluntary or involuntary actions. Overall, this study refines the understanding of striatal dysfunction in movement disorders, demonstrates that distinct neural populations underlie normal voluntary locomotion and involuntary dyskinetic movements, and defines two complementary routes for the development of symptomatic treatments.

INTRODUCTION

In the classical model of basal ganglia function, the two major anatomical pathways of the basal ganglia have opposing roles in the regulation of movement. According to the model, the activation of striatal spiny projection neurons of the direct pathway (dSPNs) elicits movement, whereas the activation of spiny projection neurons of the indirect pathway (iSPNs) suppresses movement.[1,2] Notably, the classical model provides a basic framework for understanding movement disorders, which are broadly classified into hypokinetic disorders characterized by reduced movement, such as Parkinson's disease, and hyperkinetic disorders characterized by excessive involuntary movement, such as L-DOPA-induced dyskinesias and Huntington's disease.[1–3] Physiological recordings and SPN-type specific manipulations in animal models of these conditions have yielded evidence that increased dSPN activity and/or decreased iSPN activity contributes to hyperkinetic states, whereas decreased dSPN activity and/or increased iSPN activity contributes to hypokinetic states.[1,3–10]

The classical framework also guides current clinical treatments. Hyperkinetic disorders are commonly treated using drugs intended to decrease dSPN activity and/or increase iSPN activity (*e.g.*, inhibitors of dopamine transport into synaptic vesicles, or D2-dopamine-receptor antagonists).[11] Hypokinetic disorders are commonly treated using medications intended to increase dSPN activity and/or decrease iSPN activity (*e.g.*, L-DOPA, D2-dopamine-receptor agonists).[3,7,12] Although these treatment approaches have achieved substantial success at ameliorating motor symptoms, they have notable limitations, which can include undesirable side effects, waning long-term efficacy, and applicability that is restricted to specific subpopulations of patients.[13,14] No major breakthroughs in pharmacologic treatments have emerged in over a decade, underscoring the need for deeper understanding of striatal physiology and pathophysiology in movement disorders.

One barrier to progress may be that the classical model, while valuable, does not fully capture the complexity of how the striatum contributes to the control of movement. Notably, in normal brain states, dSPNs and iSPNs exhibit approximately matching activity levels across the initiation, performance, and offset of movement, and this coordination may be important for well-choreographed motor control.[15–17]. The striatum also exhibits action-specific patterns of neural activation, in which distinct subsets of dSPNs and iSPNs jointly encode particular motor actions.[4,18]

To examine the role of such action-related striatal activity in movement disorders, here we used two-photon Ca^{2+} imaging to monitor the concurrent dynamics of dSPNs and iSPNs in head-fixed behaving mice across normal, hypokinetic, and hyperkinetic conditions, before and after treatments comprising L-DOPA, amantadine, or a combination of both drugs. We chose amantadine due to its unique clinical ability to improve both hypokinetic and hyperkinetic conditions, suggesting that its circuit-level effects might involve phenomena beyond those in the classical basal ganglia model.[14,19–21] We focused our analyses of neural activity patterns on those occurring when mice were at rest, especially at moments immediately preceding movement. This approach conferred two main benefits. First, mouse behavioral dynamics vary substantially across the multiple brain states and treatment protocols examined here, making it challenging to perform evenhanded comparisons under comparable kinematic conditions. Focusing selectively on resting periods facilitated the removal of

potentially confounding behavioral variability in analyses of neural activity. Second, in the first few seconds just prior to movement, SPN activity patterns are predictive of the upcoming action. This allowed us to study how the ongoing occurrences of these neural patterns at rest relate to an animal's overall propensity to move and how individual cells contribute to the encoding of upcoming actions.

Our analyses revealed that the subsets of SPNs encoding voluntary locomotion appear to be distinct from those encoding involuntary dyskinetic movements. Crucially, these distinct subsets of neurons were differentially affected across different pathological and treated conditions. The implication is that motor dysfunction can involve not just unbalanced striatal activity levels, as observed here and in past studies[4,8,9], but also altered rates of activity in the subsets of dSPNs and iSPNs that jointly encode specific movements. Notably, ensemble patterns of resting dSPN and iSPN activity that were predictive of upcoming voluntary locomotion were diminished under parkinsonian brain states. Moreover, both dSPNs and iSPNs encoding involuntary movements were hyperactive in dyskinetic brain states, whereas those encoding voluntary locomotion were not. Abnormal depression or potentiation of activity in the subsets of SPNs encoding specific actions may underlie these observations.

Consistent with this logic, treatment of parkinsonian mice with either L-DOPA or amantadine improved locomotor activity, but the two drugs differentially affected SPNs. L-DOPA restored the balance of striatal activity across the direct and indirect pathways, but, in contrast, amantadine preferentially enhanced the resting activity of locomotion-related dSPNs and iSPNs. Under dyskinetic states induced by high doses of L-DOPA, dSPNs were hyperactive relative to iSPNs, as in prior studies.[4,5,9] Amantadine treatment alleviated dyskinetic behavior, selectively reduced the resting activity of dyskinesia-related dSPNs and iSPNs, but did not alter the overall balance of resting dSPN and iSPN activity.

These findings challenge the notion that movement disorders arise solely from imbalances in dSPN and iSPN activity and indicate that voluntary locomotion and involuntary dyskinesia engage distinct neural populations, whose activity is altered in pathological conditions. The distinct neural ensemble level effects of amantadine versus those of L-DOPA suggest a new therapeutic approach:

rather than seeking to rebalance dSPN and iSPN activity levels, future treatments might target the specific neuronal subpopulations that drive voluntary or involuntary movements, such as by impacting neural plasticity processes.

RESULTS

Neural Ca^{2+} imaging in the dorsolateral striatum of awake, head-fixed mice

To examine the activity of SPNs during voluntary and involuntary movements, we used two-photon microscopy to image somatic SPN Ca^{2+} dynamics in head-fixed behaving mice. We used Drd1a-Cre transgenic mice, crossed with Ai14 Cre-dependent reporter mice, to selectively label dSPNs with the red fluorophore tdTomato (**Methods**).[22,23] To monitor the Ca^{2+} dynamics of both dSPNs and iSPNs, we injected AAV2/9-Camk2-jGCaMP7f virus into the dorsolateral striatum (DLS), driving expression of the green fluorescent Ca^{2+} indicator jGCaMP7f in both dSPNs and iSPNs.[24]

To gain optical access to the striatum for two-photon imaging, about a week after virus injection we implanted a gradient index (GRIN) lens over the DLS.[4,25–27] In each mouse, we recorded Ca^{2+} activity at 3 different tissue planes during each imaging session. We imaged each plane for a total duration of 20.0 min per session, parsed into two non-successive blocks of 10.0 min each, yielding a total of 60.0 min of Ca^{2+}-imaging data per session. Since dSPNs co-expressed red tdTomato and green jGCaMP7f, whereas iSPNs expressed only jGCaMP7f, dual-color two-photon imaging allowed us to distinguish these two cell types (**Figures 1A,B**). On average, we identified 371 ± 119 (mean ± s.d.) tdTomato-positive dSPNs per session, and 285 ± 179 GCaMP-positive, tdTomato-negative iSPNs per session, which led to a mean dSPN-to-iSPN cell count ratio of 1.7 ± 1.0 per session (n = 63 sessions from 6 mice). However, despite more dSPNs being identified overall, a majority of cells with detectable Ca^{2+} activity were iSPNs (78 ± 11%). We suspect this imbalance may reflect the possibility that the use of the Drd1a-Cre driver mouse line to express tdTomato in dSPNs hindered the virally driven expression of GCaMP in these cells, as a similar imbalance has been observed before with this labeling strategy.[4]

To assess mouse movement during the Ca^{2+} imaging sessions, we head-fixed mice and allowed them to run on a wheel placed under the objective lens of the two-photon microscope (**Methods**). A rotary encoder reported rotations of the wheel, which we used to determine the mouse's locomotor speed. An infrared camera captured the mouse's forelimb movements. Machine vision analyses of limb movements in the infrared videos allowed us to identify periods of involuntary dyskinetic movements, which we defined as rapid, choreiform limb movements that occurred independently of wheel motion (**Figures 1C,D**).[28] We jointly recorded neural activity and mouse behavior in each of the six different 10-min-blocks in each session. Overall, this design allowed us to track activity in the two SPN populations concurrently and to evaluate how they encode voluntary and involuntary actions across different brain states and treatment conditions **(Figure 1E)**.

Behavioral phenotypes in hypokinetic, hyperkinetic, and treated conditions

To model a hypokinetic parkinsonian state, we unilaterally lesioned the substantia nigra pars compacta (SNc) with 6-hydroxydopamine (6-OHDA) (**Supplemental Figure 1A**).[29] The lesion significantly decreased the proportion of time per block that mice engaged in locomotion as compared to pre-lesion baseline values. Treatment with either amantadine (60 mg/kg) or a standard dose of L-DOPA (1 mg/kg) led to significant improvements in the percentage of time spent ambulating per block, as compared to post-lesion, hypokinetic mice that received only saline (**Figure 1F**).

To model hyperkinetic conditions, we administered a high dosage of L-DOPA (10 mg/kg) to the same 6-OHDA-lesioned mice.[4] This induced robust choreiform movements of the forelimb contralateral to the 6-OHDA lesion, consistent with L-DOPA-induced dyskinesia (**Figures 1C,D**). Administration of amantadine, at a dosage (60 mg/kg) found previously to be effective at treating L-DOPA-induced dyskinesia in rodents,[30] together with the high dose of L-DOPA significantly reduced the percentage of time that mice exhibited dyskinetic movements (**Figure 1G**).

L-DOPA ameliorates the imbalance of dSPN to iSPN resting activity after dopamine depletion

To examine how SPN activity relates to movement, we plotted the event rates of somatic Ca^{2+} transients in dSPNs and iSPNs relative to the times of locomotion onset and offset (**Figures 2A,B**).

Before the 6-OHDA lesion of the SNc, dSPN and iSPN event rates and temporal activation patterns were similar in magnitude (**Figure 2A**). After the lesion, dSPN activity levels declined below those of iSPNs in the untreated hypokinetic condition, but treatment with L-DOPA (1 mg/kg) improved this deficit (**Figure 2B**). To quantify such observations, we computed a dSPN-to-iSPN mean activity index for both resting and pre-locomotion periods, with the latter defined as those 2-s-intervals without mouse movement, immediately prior to locomotion onset (**Methods**). Treatment with L-DOPA (1 mg/kg) but not amantadine partially restored the dSPN-to-iSPN index in both these periods (**Figures 2A**–**C**). To better understand how both L-DOPA and amantadine boosted the occurrence of locomotion, yet only L-DOPA significantly affected the dSPN-to-iSPN activity index, we examined whether the dSPN-to-iSPN index during rest influenced the probability of transitioning from rest to locomotion. Across all conditions, the pre-locomotion dSPN-to-iSPN index showed no meaningful correlation with the probability of transitioning from rest to locomotion, nor with the speed or duration of upcoming locomotion bouts, nor was it a significant predictor of these variables in linear mixed-effects model analyses (**Figure 2D, Supplemental Figure 2A**). However, both amantadine and L-DOPA (1 mg/kg) markedly affected the probability of transitioning from rest to locomotion, irrespective of the dSPN-to-iSPN index value (**Figure 2D**). These findings suggest that, although the relative activity levels of dSPNs and iSPNs may influence movement initiation, maintenance, and kinematics under certain conditions, additional mechanisms are likely involved in the regulation of locomotor behavior.

Neural activity just prior to locomotion reveals ensembles of locomotion-related neurons

To explore the relationship between SPN activity patterns immediately prior to locomotion and the speed of the mouse's upcoming locomotor bout, we employed multivariate ridge regression models (**Methods**). These models used neural activity patterns in the [–4 s, 0 s] interval just prior to locomotion onset as the predictors of subsequent locomotor speed (net R^2 = 0.91) (**Figure 3A, Supplemental Figure 2B**). Shifting the 4-s-long predictor window further back in time (*e.g.*, to the interval [–5 s, –1 s] prior to locomotion) significantly reduced the models' predictive performances

(**Supplemental Figure 2C**), suggesting that the [–4 s, 0 s] interval captured SPN activity most relevant to the upcoming locomotion. To identify neurons whose activity was predictive of upcoming changes in locomotion, we examined the regression coefficients of each SPN within each model. Neurons with regression coefficients that deviated more than +1 s.d. or less than –1 s.d. from the mean (*i.e.*, cells with z-scored regression coefficients of absolute magnitude greater than one) were classified as positive or negative locomotion-related neurons, respectively. To validate that these neurons were meaningfully related to changes in behavior, we examined the relationship between their Ca^{2+} event times and subsequent locomotor speed. Positive locomotion-related neurons were associated with significant increases in locomotor speed following their Ca^{2+} events (one-sided signed-rank test, $p < 0.001$, $n = 193$ blocks from 5 mice), whereas negative locomotion-related neurons were associated with significant decreases in locomotor speed after their Ca^{2+} events ($p = 0.03$, $n = 193$ blocks from 5 mice; **Figure 3B**). Notably, the sets of positive and negative locomotion-related neurons both had equivalent fractions of dSPNs and iSPNs (**Figure 3C**).

Amantadine rescues the decline in locomotor neuron index values in a parkinsonian state

To further examine how locomotion-related SPNs encoded upcoming motor activity, we computed a 'locomotor neuron index' that quantified the relative difference in the mean rates of Ca^{2+} events in the positive and negative locomotion-related SPN populations (**Methods**). For each experimental block, we determined values of the locomotor neuron index during the mouse's resting periods, while also assuring that these periods of rest did not overlap with the pre-locomotion intervals used to train the multivariate regression models.

In comparison to normal pre-lesion conditions, resting locomotion neuron index values were significantly reduced in the parkinsonian, hypokinetic condition following 6-OHDA lesion of the SNc (**Figures 3D,E**). Treatment with amantadine but not L-DOPA (1 mg/kg) restored values of this index to normal levels during resting periods (**Figure 3E**). Amantadine primarily increased the index values by increasing the activity of positive locomotion-related neurons (**Supplemental Figure 3A**). During pre-locomotion periods, index values were similar across all conditions, highlighting that the

relationships between locomotion-related SPNs and locomotion onset remained approximately consistent (**Figures 3D,E**).

We used a linear mixed-effects model to identify predictors of the percentage of time spent locomoting in each experimental block. This analysis revealed that the resting locomotor neuron index and the resting period activity of SPNs with positive locomotion-related coefficients were both significant predictors, whereas the resting dSPN-to-iSPN index was not (**Figure 3F, Supplemental Figure 3B**).

dSPN activity levels are elevated relative to those of iSPNs during dyskinetic brain states

During dyskinetic brain states, induced by administering high-dose L-DOPA (10 mg/kg) to 6-OHDA-lesioned mice, resting values of the dSPN-to-iSPN index were significantly elevated compared to normal, pre-lesion conditions (**Figures 4A–C**). However, the addition of amantadine to this treatment, which significantly reduced the amount of time mice exhibited dyskinetic movements (**Fig. 1G**), did not normalize the dSPN-to-iSPN index values (**Figures 4B,C**). Further, resting periods with high dSPN-to-iSPN index values had only modestly higher probabilities of transitioning from rest to dyskinesia than those with low dSPN-to-iSPN index values (**Figure 4D**). Lastly, dSPN-to-iSPN index values in 2-s-intervals immediately prior to bouts of dyskinesias did not correlate with either the speed or duration of the upcoming dyskinesia, nor did the values of this index significantly predict dyskinesia speed or duration in a linear mixed-effects model (**Supplemental Figure 4A**).

Neural activity patterns just prior to dyskinesia reveal dyskinesia-related neurons

To examine the relationships between the SPN activity patterns immediately preceding bouts of dyskinesia and the extent of dyskinetic movements, we again employed multivariate regression models. We created models for each block for each mouse, with the activity of individual SPNs in the [–4 s, 0 s] intervals preceding dyskinesia onset serving as predictors. Across all mice and both hyperkinetic conditions (high-dose L-DOPA (10 mg/kg) and high-dose L-DOPA + amantadine), the models significantly predicted dyskinesia forelimb speeds (net R^2 = 0.59; **Figure 5A, Supplemental Figure 4B**), although the predictive performances were lower than those of our locomotion models

(**Figure 3A**). Similarly to the locomotion models, shifting the analysis window backwards in time from the onset of dyskinesia reduced the models' predictive capabilities, supporting the relevance of SPN activity in the [–4 s, 0 s] interval to dyskinesia (**Supplemental Figure 4C**).

Analogous to our analyses of locomotion models, from the dyskinesia models we identified SPNs with positive regression coefficients (z-score > +1) and classified them as positive dyskinesia-related neurons. Ca^{2+} events in these neurons were significantly associated with increases in contralateral forelimb speed (one-sided signed-rank test, $p = 0.02$, $n = 111$ blocks from 6 mice; **Figure 5B**). In comparison, Ca^{2+} events in SPNs with negative regression coefficients (z-score < –1) in the dyskinesia regression models were not associated with reductions in dyskinetic forelimb speed (one-sided signed-rank test, $p > 0.05$, $n = 111$ blocks from 6 mice; **Figure 5B**). Thus, we focused subsequent analyses on positive dyskinesia-related neurons. This subset of cells comprised both dSPNs and iSPNs, although dSPNs were overrepresented compared to their proportion in the overall population of recorded neurons (**Figure 5C**).

Notably, amantadine treatment selectively reduced the Ca^{2+} transient event rates of positive dyskinesia-related neurons during resting but not pre-dyskinesia periods (**Figures 5D,E**). This suggests that while amantadine seems to reduce the baseline activity of these neurons, it may not alter their relationship with dyskinesia. Notably, the resting Ca^{2+} transient rates of positive dyskinesia-related neurons were predictive of the amount of dyskinesia per block (**Figure 5F**), whereas neither resting dSPN-to-iSPN index values nor resting dSPN activity predicted dyskinesia levels. Finally, amantadine treatment altered neither the amount of locomotion per block, nor resting values of the locomotor neuron index, nor the resting Ca^{2+} event rates of positive locomotion-related neurons (**Figure 5G**, **Supplemental Figure 5A**). These findings suggest that, under hyperkinetic conditions, amantadine preferentially affected the set of positive dyskinesia-related neurons.

Dyskinesia- and locomotion-related SPNs are distinct neural ensembles with distinct dynamics

To compare the neural representations of voluntary and involuntary movements, we focused on experimental time blocks that had separate bouts of locomotion and dyskinesia. Examining the activity

of positive dyskinesia- and positive locomotion-related neurons, we found that an index characterizing the relative activity of these two populations was, as expected, higher in intervals preceding dyskinesia than those preceding locomotion, supporting our cell classifications (**Figures 6A–C**; **Methods**). The more generic dSPN-to-iSPN activity index also had higher values during intervals preceding dyskinesia (**Figure 6C**), in accord with prior studies.[4,9] Of note, across the population of SPNs, regression coefficients for dyskinesia- and locomotion-related cells were largely uncorrelated (R^2 = 0.01 across all mice; **Figure 6D**). Although we independently classified neurons as positive locomotion- and positive dyskinesia-related, only a limited subset of cells had both classifications (9.3 ± 10.5%; mean ± s.d.; n = 41 blocks with L-DOPA (10 mg/kg) treatment with both locomotion and dyskinesia bouts; 519 positive locomotion- and/or dyskinesia-related neurons across 6 mice).

To determine whether locomotion and dyskinesia are represented as distinct neural states, we created support vector machine (SVM) decoders of neural ensemble activity to classify behavioral states. These decoders accurately distinguished periods of locomotion and dyskinesia with high classification accuracy across all mice, with relatively minimal misclassifications of these behaviors (**Figure 7A**, **Supplemental Figure 6A**). Consistent with this, time series visualizations of decoder outputs showed clear separations between epochs of locomotion and dyskinesia, confirming that these behaviors are associated with clearly distinguishable patterns of striatal activity (**Figure 7B**, **Supplemental Figure 7A**). Altogether, these observations indicate that the dorsolateral striatum has distinct neural ensemble representations of locomotion and dyskinesia.

DISCUSSION

The striatum plays a central role in motor control, integrating inputs from cortical, thalamic, and dopaminergic sources to guide actions.[31] The classical view of striatal function emphasizes the opposing roles of dSPNs and iSPNs in promoting and inhibiting movement, respectively.[1,7] Although this framework has provided valuable insights into basal ganglia function and dysfunction, it seemingly fails to capture the full complexity of striatal representations of movement. dSPNs and iSPNs exhibit

coordinated, action-specific patterns of neural activity, reflecting that the direct and indirect pathways appear to act concertedly to shape motor output.[15–18]

Our study extends this idea to pathological motor states, which we found were associated with alterations in both dSPN/iSPN balance and action-specific patterns of SPN activity. In hypokinetic brain states, dSPN activity was reduced relative to iSPN activity, as was a measure of the activity of locomotion-related dSPNs and iSPNs (**Figures 2C**, **3E**). L-DOPA partly restored the dSPN/iSPN activity balance (**Figure 2C**). By comparison, amantadine primarily enhanced the resting activity of locomotion-related SPNs, which was associated with the percentage of time spent ambulating (**Figures 3E,F**). Under hyperkinetic conditions, characterized by L-DOPA-induced dyskinesias, we observed a relative elevation of mean dSPN over mean iSPN activity levels (**Figure 4C**). Although amantadine reduced dyskinesias, it did not reduce the dSPN/iSPN imbalance (**Figures 1G, 4C**). Rather, it selectively suppressed the resting activity of dyskinesia-related SPNs, which correlated with the percentage of time mice exhibited dyskinesias (**Figures 5E,F**).

Of note, dyskinesia- and locomotion- related neural ensembles were largely distinct and comprised both dSPNs and iSPNs (**Figures 3C, 5C, 6D**). A recent preprint by the Costa lab presents complementary findings, showing that different types of dyskinesias are associated with the activity of different sets of both dSPNs and iSPNs.[32] Together, these findings suggest that abnormal activity levels of specific action-related SPN ensembles contribute to both hypokinetic and hyperkinetic conditions. Hence, modulating the activity of these specific neurons in patients with movement disorders might represent a viable, alternative therapeutic strategy complementing efforts to rebalance dSPN/iSPN activity levels. To advance this proposed treatment approach, a next step could be to establish methods for identifying and evaluating candidate interventions that normalize the activity of action-related SPNs under pathologic conditions. A contribution of our study is the development of an assay that might allow such screening by combining joint imaging of dSPN and iSPN activity with automated behavioral analyses.

One approach to find initial candidates for screening could involve taking inspiration from amantadine, a clinically effective drug for movement disorders known to act on a diverse set of

molecular targets.[14,20] Although our study did not determine which of amantadine's targets mediate its ensemble-specific effects, our results allow us to generate hypotheses. Two key targets of interest are NMDA receptors and Kir2 potassium channels.[14,19,33] NMDA receptors have an important role in corticostriatal plasticity, which seems to be impaired in parkinsonian and dyskinetic brain states.[34–37] Amantadine's NMDA receptor antagonism might limit long-term potentiation (LTP) at corticostriatal synapses onto action-related SPN populations, potentially reducing maladaptive plasticity and subsequent pathological activity levels in these specific neurons.[14,33] However, amantadine's antagonism of Kir2 receptors appears to enhance the excitability of both iSPNs and dSPNs, which seems to enhance LTP induction in iSPNs without affecting LTP in dSPNs.[19] This disparity might serve to rebalance activity levels between action-related SPNs with pathologic activity levels and the rest of the SPN population. Based on these possible mechanisms, future work could explore targeted modifications of amantadine's pharmacological mechanisms of action to bias its effects toward specific receptor classes.[38] By evaluating whether candidate interventions improve behavioral measures and normalize striatal dynamics, drug compounds might be advanced with greater confidence from preclinical to clinical development, accelerating the search for more effective treatments of movement disorders.

Limitations of the study

Our study has several limitations. First, it only focuses on one hypokinetic condition (severe acute unilateral dopamine depletion via 6-OHDA) and one hyperkinetic condition (L-DOPA-induced dyskinesias in unilateral dopamine-depleted mice). These models, while widely used, do not fully capture the complexity of human movement disorders, and our findings may not generalize to other hypokinetic and hyperkinetic movement disorders.

Second, although we identified neural populations with activity that correlated with specific behaviors, we did not directly manipulate the activity of these populations. Thus, we cannot establish definitive causal links between their activity patterns and observed behavioral changes. However, by focusing our analyses on resting and pre-movement periods, we aimed to minimize the confounding

influence of ongoing movement dynamics, strengthening interpretations that these neural populations are involved in the initiation of voluntary and involuntary movements. We also conducted analyses of SPN activity patterns during resting intervals that were separate from the pre-movement intervals used to identify neurons with particular coding attributes. Findings that the resting activity levels of movement-related neurons were related to the characteristics of upcoming movement bouts further speak to the likely relevance of these cells to action specification.

Third, we did not track longitudinally the activity of individual neurons across experimental conditions. Instead, for experimental convenience, we identified action-related SPNs separately for each brain state and treatment condition. However, this experimental choice limited our ability to determine whether individual neurons had consistent functional roles across the different contexts. To address these three limitations, future studies should examine additional movement disorder models, perform targeted manipulations of specific neurons such as with optogenetic or chemogenetic methods, and longitudinally track individual SPNs across different brain states and treatments.

AUTHOR CONTRIBUTIONS

G.C. and M.J.S. conceived the study and designed data analyses. G.C. performed behavioral and imaging experiments, surgeries, and data analyses. R.C. built the microscope and created the software to control the microscopy and behavioral apparatus. J.L. bred transgenic mice and performed immunohistochemistry. Y.Z. designed and performed viral vector subcloning and virus validation. G.C. and M.J.S. wrote the manuscript. All authors edited the paper. M.J.S. supervised the study.

RESOURCE AVAILABILITY

Lead contact

Further information and requests for resources should be directed to lead contact Mark J. Schnitzer (mschnitz@stanford.edu).

Materials availability

This study did not generate new unique reagents.

Data and code availability

All data and code used in this paper are available from the lead contact upon request.

ACKNOWLEDGEMENTS

G.C. thanks B. Ahanonu, T. Rogerson, F. Dinc, and O. Hazon for technical advice regarding rodent surgeries and data analyses. This study was supported by an American Academy of Neurology Neuroscience Research Training Scholarship (G.C.), the Chan Zuckerberg Biohub Physician Scientist Fellowship Program (G.C.), the Stanford Knight Initiative for Brain Resilience (M.J.S.), the Ludwig Foundation (M.J.S.), and a Department of Defense Vannevar Bush Faculty Fellowship (M.J.S.).

Figure 1

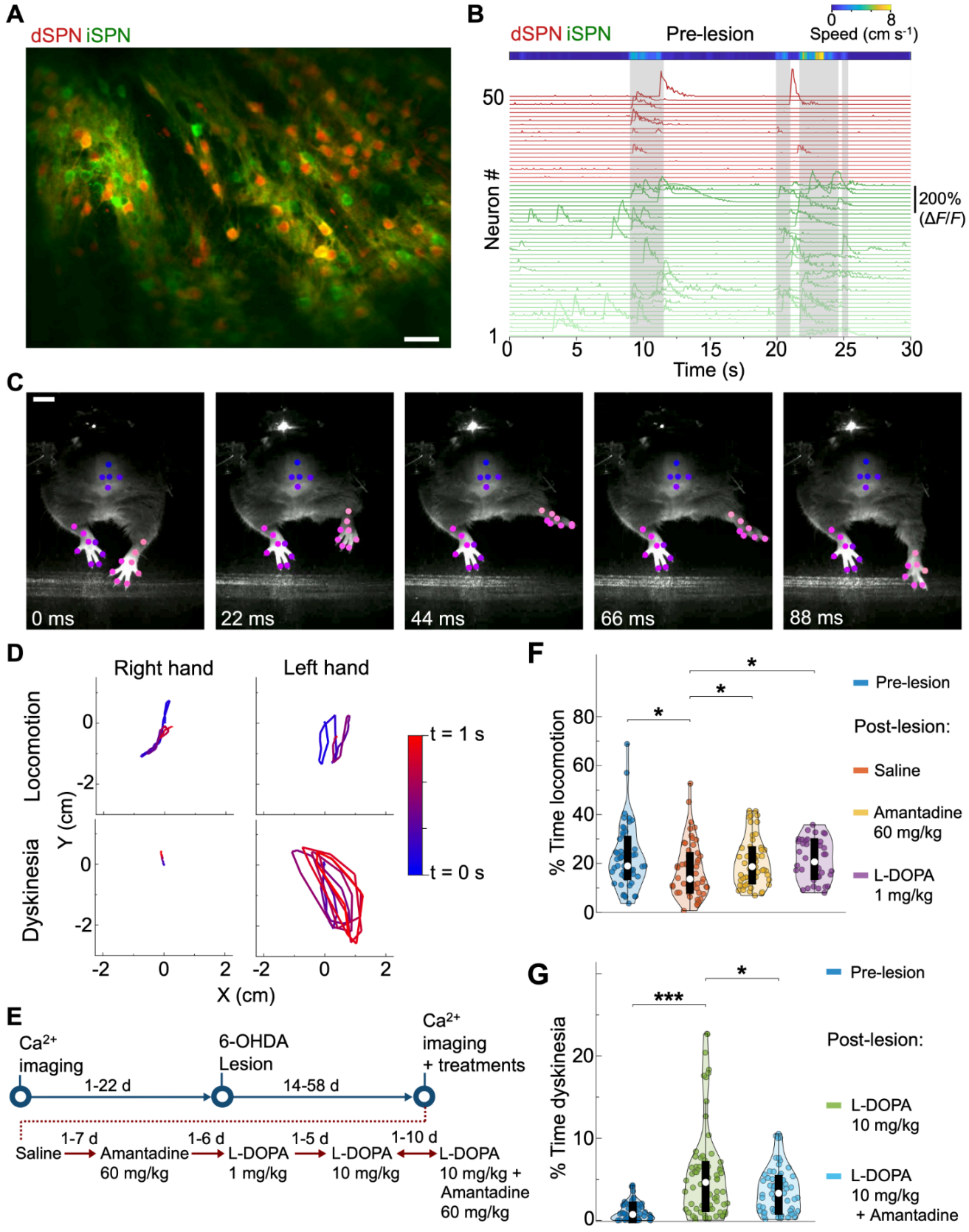

Figure 1. Imaging SPN Ca^{2+} activity and analysis of movement kinematics in awake mice across normal, hypokinetic, hyperkinetic, and treated conditions.

(A) Example dual-color image of SPNs acquired by two-photon microscopy via a GRIN lens. dSPNs but not iSPNs expressed red fluorescent tdTomato. Both SPN-types expressed green jGCaMP7f. The image is a time-averaged projection of a movie lasting 10 min. Gray shading marks periods of locomotion. Scale bar: 40 μm.

(B) *Bottom*, Example traces of fluorescence Ca^{2+} activity ($\Delta F/F$) of individual dSPNs (red traces) and iSPNs (green traces), recorded concurrently in a normal mouse. *Top*, Color plot of the mouse's locomotor speed on the wheel.

(C) Representative sequence of image frames acquired by infrared videography, showing one phase of a rapid raising movement of the left forepaw, which was subsequently repeated (see **D**). This movement pattern was characteristic of L-DOPA-induced dyskinesia contralateral to a 6-OHDA lesion in the substantia nigra pars compacta (SNc). Colored dots denote body parts that were tracked using the machine vision analysis package, DeepLabCut.[28] Different color dots denote different body parts (*e.g.*, right hand, left hand). Scale bar: 1 cm.

(D) Traces of right and left forepaw movements (1-s-durations) in the two dimensions captured by infrared videography (90 fps) during representative bouts of locomotion (*top row*) and dyskinesia (*bottom row*). Color scale shows the time elapsed following movement initiation.

(E) Experimental timeline for pre-lesion Ca^{2+} imaging and behavioral tracking sessions, 6-OHDA injection, and post-lesion Ca^{2+} imaging and behavioral testing sessions. We administered drug treatments in the order shown. After an imaging session with L-DOPA (1 mg/kg), sessions alternated between administration of either L-DOPA (10 mg/kg) or L-DOPA (10 mg/kg) + amantadine.

(F) Violin plots showing the percentage of time in each block that mice spent in locomotor behavior. Compared to before the 6-OHDA lesion, in the untreated hypokinetic condition we observed a decline

in the time spent in locomotion, which was improved by both amantadine and L-DOPA (1 mg/kg) treatment. (*$p < 0.05$; two-sided rank sum tests, corrected for multiple comparisons using a Benjamini–Hochberg procedure with a false-discovery rate of 0.05; n = 50 pre-lesion blocks, 53 saline blocks, 53 amantadine blocks, and 38 L-DOPA (1 mg/kg) blocks from 5 mice).

(G) Violin plots of the percentage of time in each block that mice exhibited dyskinetic movement. The addition of amantadine to high-dose L-DOPA (10 mg/kg) led to reduced dyskinesia. The low levels of machine-vision-detected 'dyskinesias' in pre-lesion blocks in actuality reflect grooming or other spontaneous non-locomotor movements. (*$p < 0.05$, **$p < 0.01$, ***$p < 0.001$; one-sided rank sum tests, corrected for multiple comparisons using a Benjamini–Hochberg procedure with a false-discovery rate of 0.05; n = 56 pre-lesion blocks, 57 L-DOPA (10 mg/kg) blocks, and 56 L-DOPA (10 mg/kg) + amantadine blocks from 6 mice).

Here, and in violin plots throughout the paper, each violin shows a distribution of data for a given experimental condition, with the violin width denoting the probability density. The white dot in each violin marks the median value, the thick black box marks the interquartile range (IQR: 25th–75th percentiles), and the thin black lines extend to 1.5 times the IQR or the furthest data point within the IQR. Colored dots are individual data points.

Figure 2

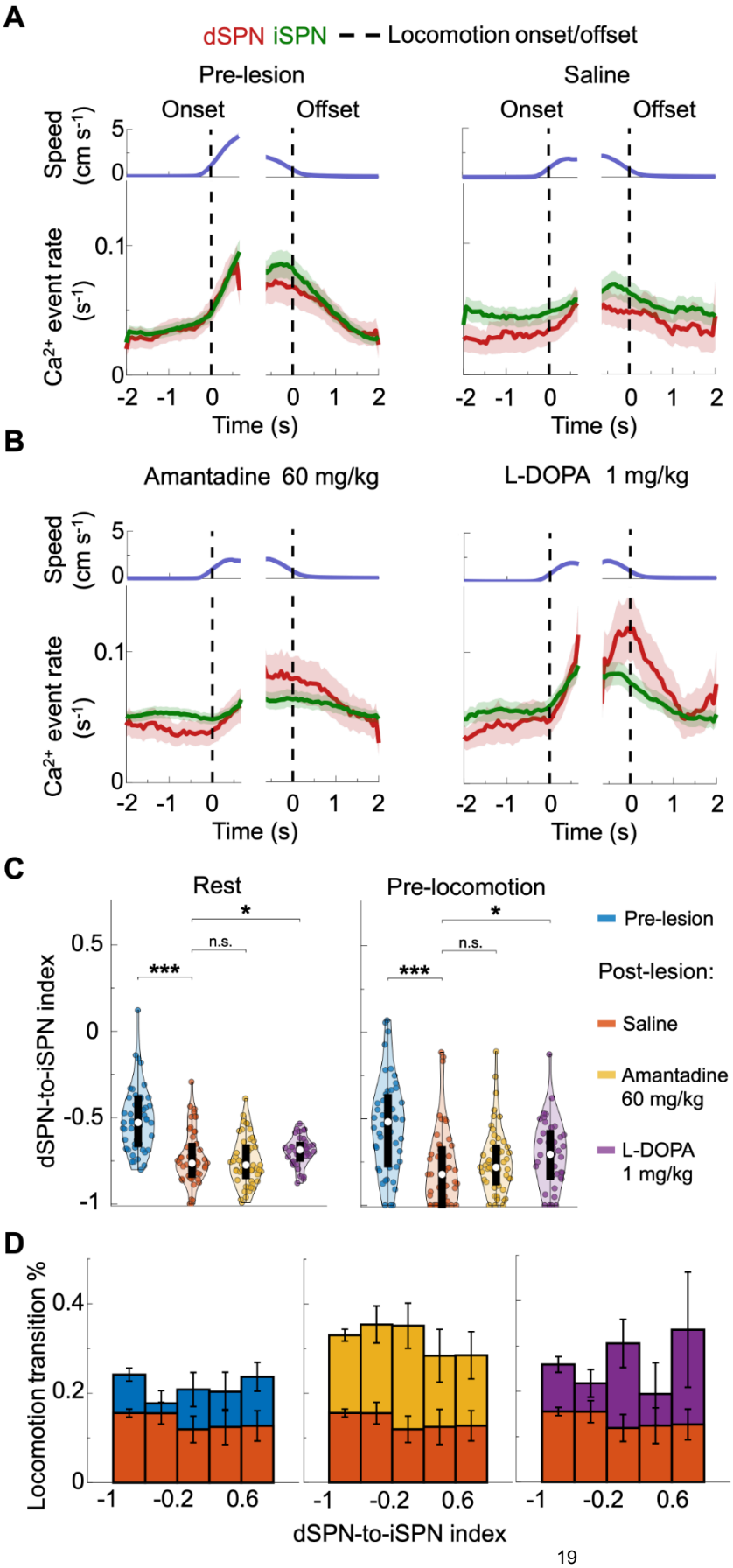

Figure 2. L-DOPA ameliorates the imbalance of dSPN to iSPN resting activity during hypokinetic conditions.

(A) *Top,* Mean locomotor speed, plotted relative to times of locomotor onset and offset (vertical dashed lines), before (*left*) or after (*right*) unilateral dopamine lesion of the SNc. *Bottom*, Ca^{2+} event rates of dSPNs and iSPNs plotted relative to locomotion onset and offset, shown for each condition. Colored shading: s.e.m. for n = 50 pre-lesion and 53 saline blocks from 5 mice.

(B) Analogous plots to those of **A**, for mice administered either amantadine or L-DOPA (1 mg/kg) after the dopamine lesion. Colored shading: s.e.m. for n = 53 amantadine blocks and 38 L-DOPA blocks, from 5 mice.

(C) Violin plots showing the distributions of dSPN-to-iSPN index values before and after the lesion, during resting (*left*) and pre-locomotion periods (*right*). L-DOPA (1 mg/kg) but not amantadine elevated the index values following the lesion. (*$p < 0.05$, **$p < 0.01$, ***$p < 0.001$; n.s. = not significant; two-sided rank sum tests corrected for multiple comparisons using a Benjamini–Hochberg procedure with a false-discovery rate of 0.05; n = 50 pre-lesion blocks, 53 saline blocks, 53 amantadine blocks, and 38 L-DOPA blocks from 5 mice). Color legend also applies to **D**.

(D) Bar plots showing the probabilities of transitioning from rest to locomotion as a function of the dSPN-to-iSPN index in mice at rest. Pre-lesion, amantadine, and L-DOPA (1 mg/kg) conditions displayed significantly higher transition probabilities across all index bins as compared to the saline condition. Error bars: s.e.m. estimated based on counting statistics for a binomial distribution (**Methods**). ($p < 0.05$; one-sided signed-rank tests corrected for multiple comparisons using a Benjamini–Hochberg procedure with a false-discovery rate of 0.05; n = 6 bins from 5 mice).

Figure 3

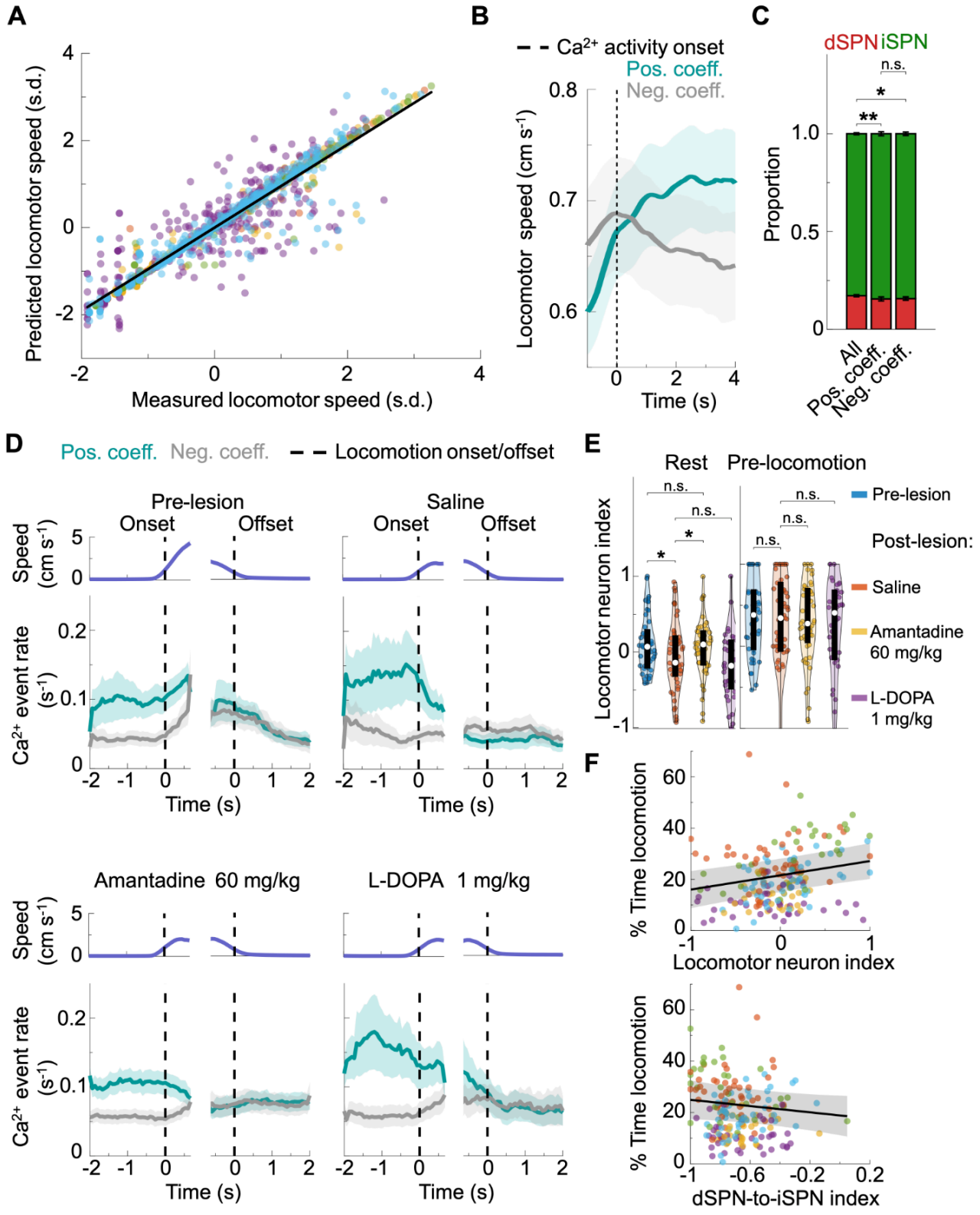

Figure 3. Locomotion-related neurons consist of dSPNs and iSPNs, are modulated by amantadine, and have resting activity levels that are predictive of locomotion bouts.

(A) Results of a multivariate ridge regression analysis predicting the speed of upcoming locomotion bouts based on the neural activity patterns just prior to movement. The scatter plot shows predicted *vs*. measured locomotion speeds for 5 mice, color-coded by mouse. Each data point shows results for an individual bout of locomotion. Speeds are z-scored for each mouse. The overall regression line (black) has a net R^2 of 0.91 and a slope of 0.95. Data in panels (**A–C**, **F**) are pooled across the 4 conditions shown in (**D**).

(B) Mean locomotion speed relative to the time of Ca^{2+} events for neurons with positive or negative coefficients in the ridge regression model of (**A**), averaged across all Ca^{2+} events. Activation of positive coefficient (teal) or negative coefficient (gray) neurons was associated with an increase or decrease in locomotion speed, respectively. Shading: s.e.m. for n = 193 experimental blocks comprising 50 pre-lesion blocks, 53 saline blocks, 53 amantadine blocks, and 37 L-DOPA (1 mg/kg) blocks from 5 mice. Dashed vertical line: Ca^{2+} event onset (t = 0).

(C) Proportions of dSPNs and iSPNs across the sets of all neurons, positive coefficient locomotion neurons, and negative coefficient locomotion neurons (*p < 0.05, **p < 0.01; n.s. = not significant; two-sided rank sum tests corrected for multiple comparisons using a Benjamini–Hochberg procedure with a false-discovery rate of 0.05; n = 193 experimental blocks comprising 50 pre-lesion blocks, 53 saline blocks, 53 amantadine blocks, and 37 L-DOPA (1 mg/kg) blocks from 5 mice). Error bars: s.e.m.

(D) *Upper*, plots of mean locomotor speed, and *lower*, mean Ca^{2+} event rates of positive- and negative-coefficient locomotion neurons, aligned to locomotion onset and offset across the 4 different conditions shown. Shading: s.e.m. for n = 50 pre-lesion blocks, 53 saline blocks, 53 amantadine blocks, and 37 L-DOPA (1 mg/kg) blocks, from 5 mice.

(E) Violin plots of the mean resting and pre-locomotion period locomotor neuron index per block, for 4 different brain states or treatment conditions. Amantadine but not L-DOPA (1 mg/kg) improved the resting locomotor neuron index. Statistical comparisons were performed using rank sum tests (*$p < 0.05$; n.s. = not significant; n = 50 pre-lesion blocks, 53 saline blocks, 53 amantadine blocks, and 37 L-DOPA (1 mg/kg) blocks from 5 mice). For the two significant comparisons, one-sided rank sum tests were used. For the non-significant (n.s.) comparisons, one-sided tests in each direction confirmed non-significance. Tests were corrected for multiple comparisons using a Benjamini–Hochberg procedure with a false-discovery rate of 0.05.

(F) Linear mixed-effects models show that the locomotor neuron index predicts the time spent in locomotion (slope = 5.6, $p < 0.001$), whereas the dSPN-to-iSPN index does not (slope = –6.1, $p = 0.12$). Points in the scatter plots denote data from individual blocks, color-coded by individual mice, with regression lines fit for the untreated hypokinetic (saline control) condition (n = 193 blocks from 5 mice).

Figure 4

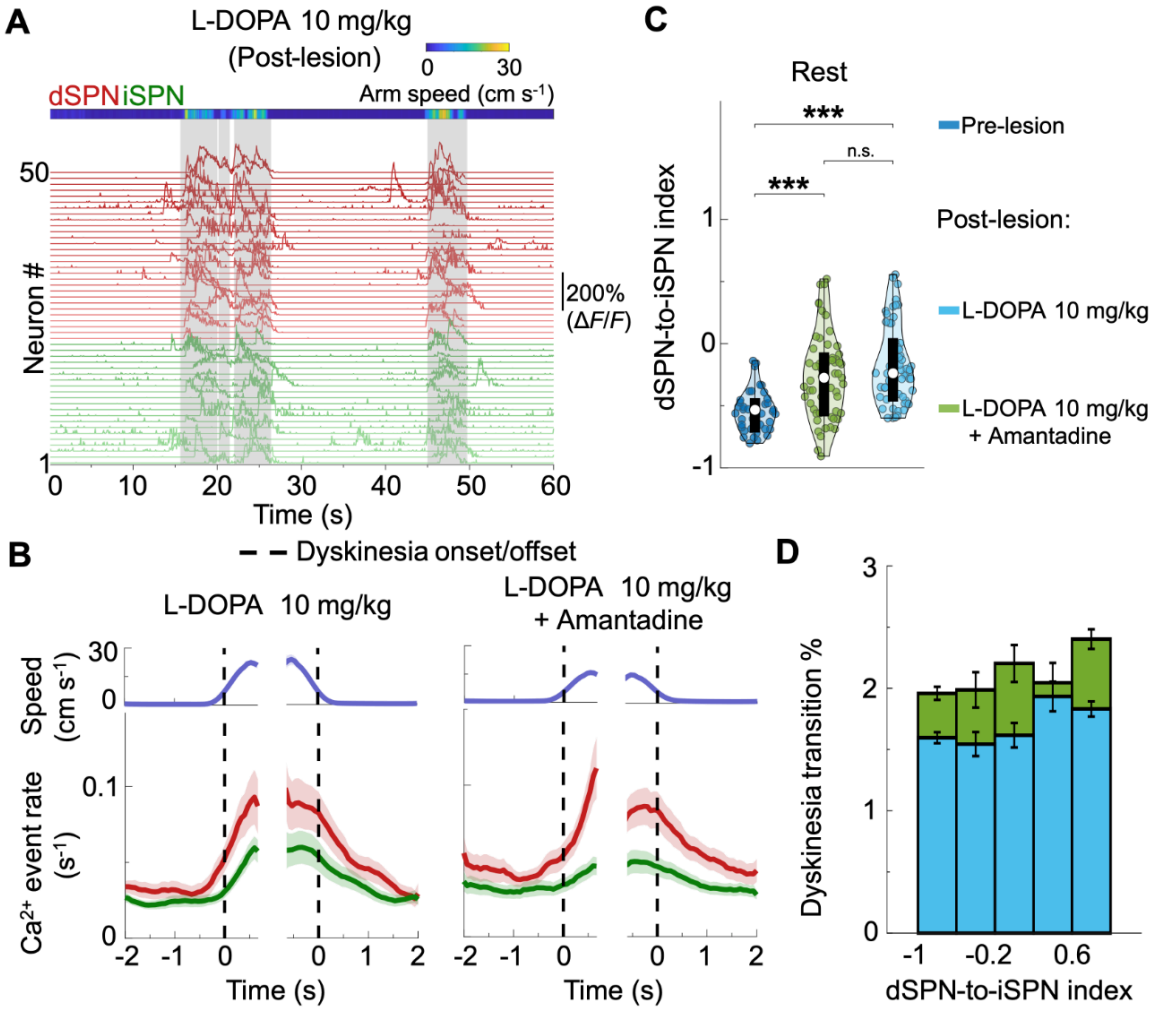

Figure 4. The dSPN-to-iSPN index is increased in the hyperkinetic condition and is unaffected by amantadine.

(A) *Bottom*, Example Ca^{2+} activity traces ($\Delta F/F$) of individual dSPNs (red) and iSPNs (green) recorded simultaneously during a L-DOPA (10 mg/kg) block. *Top*, Color plot of left forelimb speed during dyskinetic movements (marked with gray shading).

(B) *Lower,* mean Ca^{2+} event rates of dSPNs (red) and iSPNs (green), aligned to dyskinesia onset and offset, shown for two treatment conditions. *Upper*, plots of mean forelimb speed. Shading: s.e.m. for n = 57 L-DOPA (10 mg/kg) blocks, and 55 L-DOPA (10 mg/kg) + amantadine blocks from 6 mice.

(C) Violin plots of resting period dSPN-to-iSPN index values in individual experimental blocks, across three different conditions. (***$p < 0.001$; n.s. = not significant; two-sided rank sum tests corrected for multiple comparisons using a Benjamini–Hochberg procedure with a false-discovery rate of 0.05; n = 56 pre-lesion blocks, 57 L-DOPA (10 mg/kg) blocks, and 55 L-DOPA (10 mg/kg) + amantadine blocks from 6 mice). Color legend also applies to **D**.

(D) Bar plots showing the probability of transitioning from rest to dyskinesia relative to the dSPN-to-iSPN index of the rest period. The L-DOPA (10 mg/kg) condition had a significantly higher dyskinesia transition probability across all dSPN-to-iSPN index bins than the L-DOPA (10 mg/kg) + amantadine condition ($p < 0.05$; one-sided signed-rank test; n = 6 bins from 6 mice). Error bars: s.e.m. estimated using counting statistics for a binomial distribution (**Methods**).

Figure 5

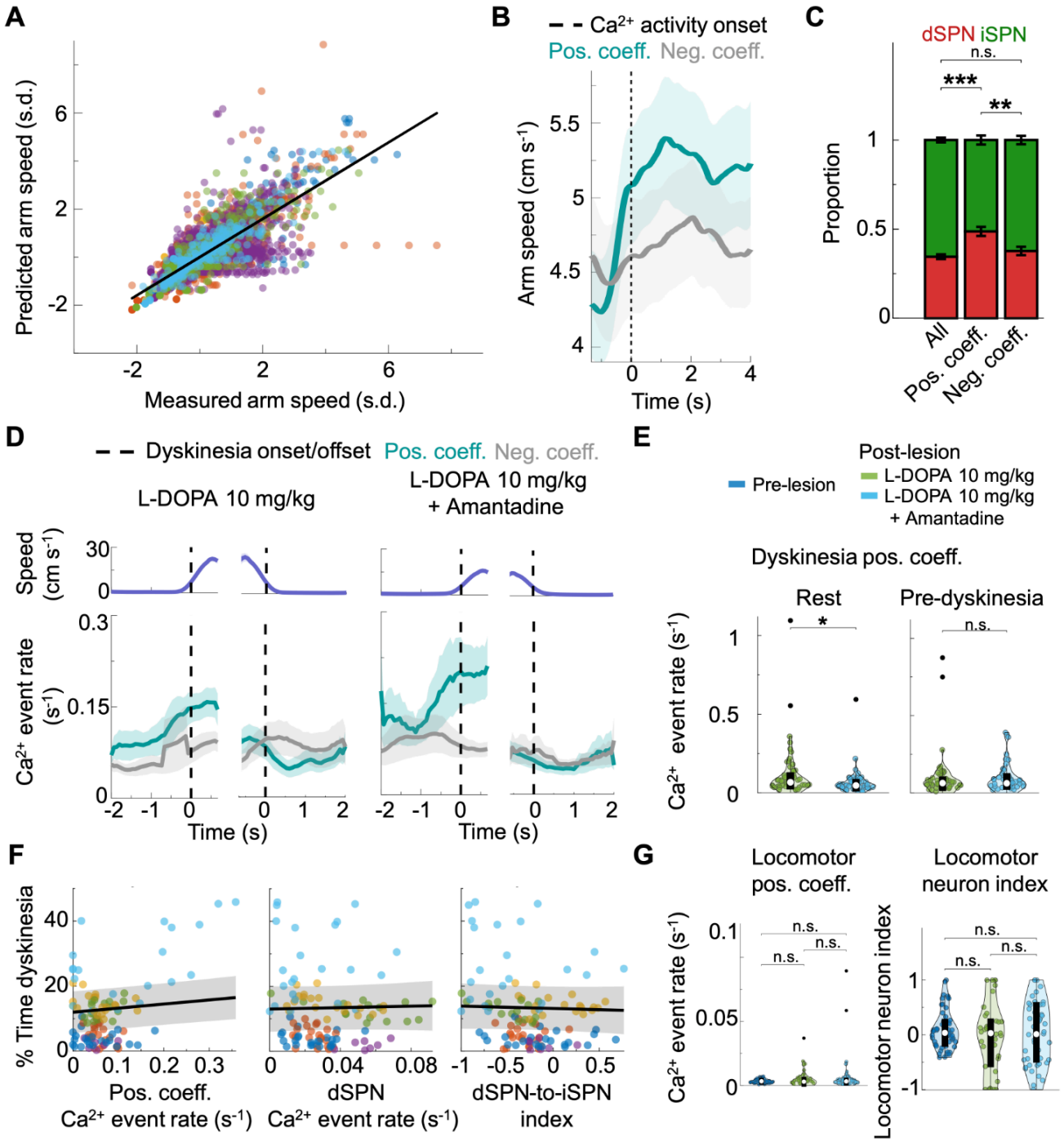

Figure 5. Positive dyskinesia-related neurons consist of dSPNs and iSPNs and are selectively modulated by amantadine.

(A) Results of a multivariate ridge regression predicting the speed of upcoming left forelimb movement, based on neural activity patterns just prior to dyskinetic movement. The scatter plot shows predicted *vs*. measured left forelimb speeds across 6 mice, color-coded by mouse. Each data point shows results for an individual dyskinetic movement. Speeds are z-scored for each mouse. The overall regression line (black) shows the model's predictive performance, with an R^2 of 0.59 and slope of 0.8. One outlier point (x = 1.65, y = 16.6) is not plotted to avoid visual distortion of the plot. Data in (**A–C**, **F**) are pooled across the two different treatment conditions shown in (**D**), L-DOPA (10 mg/kg) and L-DOPA (10 mg/kg) + amantadine.

(B) Mean speed of left forelimb movement relative to the time of Ca^{2+} events for neurons with positive and negative coefficients from the ridge regression model in (**A**), aggregated across all Ca^{2+} events. Although the activity of positive coefficient neurons (teal) was associated with an increase in dyskinesia forelimb speed, the activity of negative coefficient neurons was not associated with a decrease in dyskinesia forelimb speed. Hence, subsequent analyses focused on positive dyskinesia-related neurons. Shading: s.e.m. for n = 111 experimental blocks, comprising 57 L-DOPA (10 mg/kg) blocks and 54 L-DOPA (10 mg/kg) + amantadine blocks from 6 mice. Dashed vertical line: Ca^{2+} event onset (t = 0).

(C) Proportions of dSPNs and iSPNs across the sets of all neurons, positive coefficient dyskinesia neurons, and negative coefficient dyskinesia neurons. (**p < 0.01, ***p < 0.001; n.s. = not significant; two-sided rank sum tests corrected for multiple comparisons using a Benjamini–Hochberg procedure with a false-discovery rate of 0.05; n = 111 experimental blocks, comprising 57 L-DOPA (10 mg/kg) blocks and 54 L-DOPA (10 mg/kg) + amantadine blocks from 6 mice). Error bars: s.e.m.

(D) *Lower,* Mean Ca^{2+} event rates of positive and negative coefficient dyskinesia neurons aligned to dyskinesia onset and offset. *Upper*, plots of mean forelimb speed. Shading: s.e.m. for n = 57 L-DOPA (10 mg/kg) blocks, and 54 L-DOPA (10 mg/kg) + amantadine blocks from 6 mice.

(E) Violin plots of mean Ca^{2+} event rate during resting (*left*) and pre-dyskinesia (*right*) periods for positive dyskinesia-related neurons in individual experimental blocks. Black points: outliers >3 s.d. from the mean. (*p < 0.05; n.s. = not significant; two-sided rank sum tests; 57 L-DOPA (10 mg/kg) blocks, 54 L-DOPA (10 mg/kg) + amantadine blocks from 6 mice).

(F) Linear mixed-effects models reveal relationships between the percentage of time spent in dyskinesia in individual experimental blocks, the rate of Ca^{2+} events during resting periods for positive dyskinesia-related neurons (*left*, slope = 12.6, p = 0.002), the rate of dSPN Ca^{2+} events (*middle*, slope = 11.1, p = 0.712), or the resting dSPN-to-iSPN index (*right*, slope = –0.73, p = 0.615) across behavioral conditions. Scatter plots show individual blocks, color-coded by individual mice, with regression lines fit for the L-DOPA (10 mg/kg) condition. The x-axis is clipped at 3 s.d. from the mean to avoid visual distortion of the plot owing to a small number (1 to 3 per plot) of outlier data points (n = 111 blocks from 6 mice).

(G) Violin plots of the mean resting period Ca^{2+} event rates for positive locomotion-related neurons and the locomotor neuron index (**Methods**) per block across conditions. Legend in (**E**) also applies to (**G**). Black points: outliers > 3 s.d. from the mean. (n.s. = not significant; two-sided rank sum tests, 56 pre-lesion blocks, 57 L-DOPA (10 mg/kg) blocks, 55 L-DOPA (10 mg/kg) + amantadine blocks from 6 mice).

Figure 6

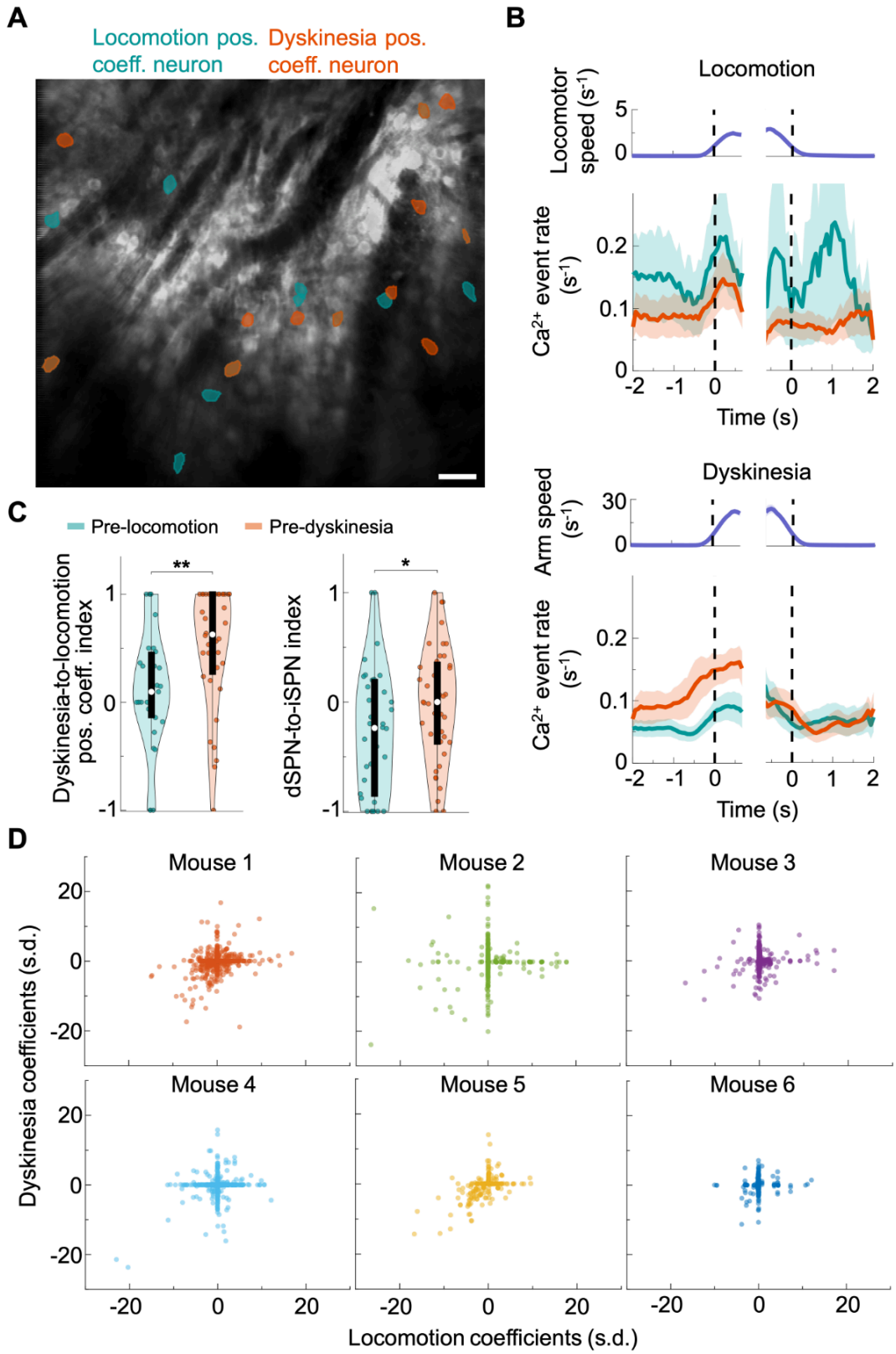

Figure 6. Locomotion- and dyskinesia-related neurons are largely distinct subsets.

(A) Example fluorescence image of striatal neurons visualized by two-photon microscopy via a GRIN lens. Masks for positive locomotion- and positive dyskinesia-related neurons are overlaid on the image to illustrate their spatial distribution. The image is a time-averaged projection of a 10 min Ca^{2+} video taken in the L-DOPA (10 mg/kg) condition. Scale bar: 40 μm.

(B) *Lower,* Mean Ca^{2+} event rates of positive locomotion- and positive dyskinesia-related neurons, aligned to movement onset and offset during L-DOPA (10 mg/kg) blocks**.** *Upper*, plots of mean locomotion speed. Vertical dashed lines mark the times of movement onset and offset. Shading: s.e.m. for n = 41 blocks from 6 mice.

(C) *Left*, Violin plots of the mean dyskinesia-to-locomotion positive coefficient index during time windows that preceded either locomotion (teal) or dyskinesia (orange) bouts. This index is a measure of the relative activity of positive dyskinesia- to positive locomotion-related neurons (**Methods**). *Right*, Violin plots of the dSPN-to-iSPN index for time windows preceding either locomotion or dyskinesia bouts. (*$p < 0.05$, **$p < 0.01$; two-sided rank sum tests; n = 41 L-DOPA (10 mg/kg) blocks with both locomotion and dyskinesia bouts from 6 mice).

(D) Scatter plot showing normalized locomotion and normalized dyskinesia coefficients across 6 individual mice. Each point denotes data from a single neuron. The low R^2 values across mice (Mouse 1: 0.06, Mouse 2: 0.01, Mouse 3: 0.02, Mouse 4: 0.07, Mouse 5: 0.33, Mouse 6: 0.01) indicate that locomotion- and dyskinesia-related neurons are largely distinct populations.

Figure 7

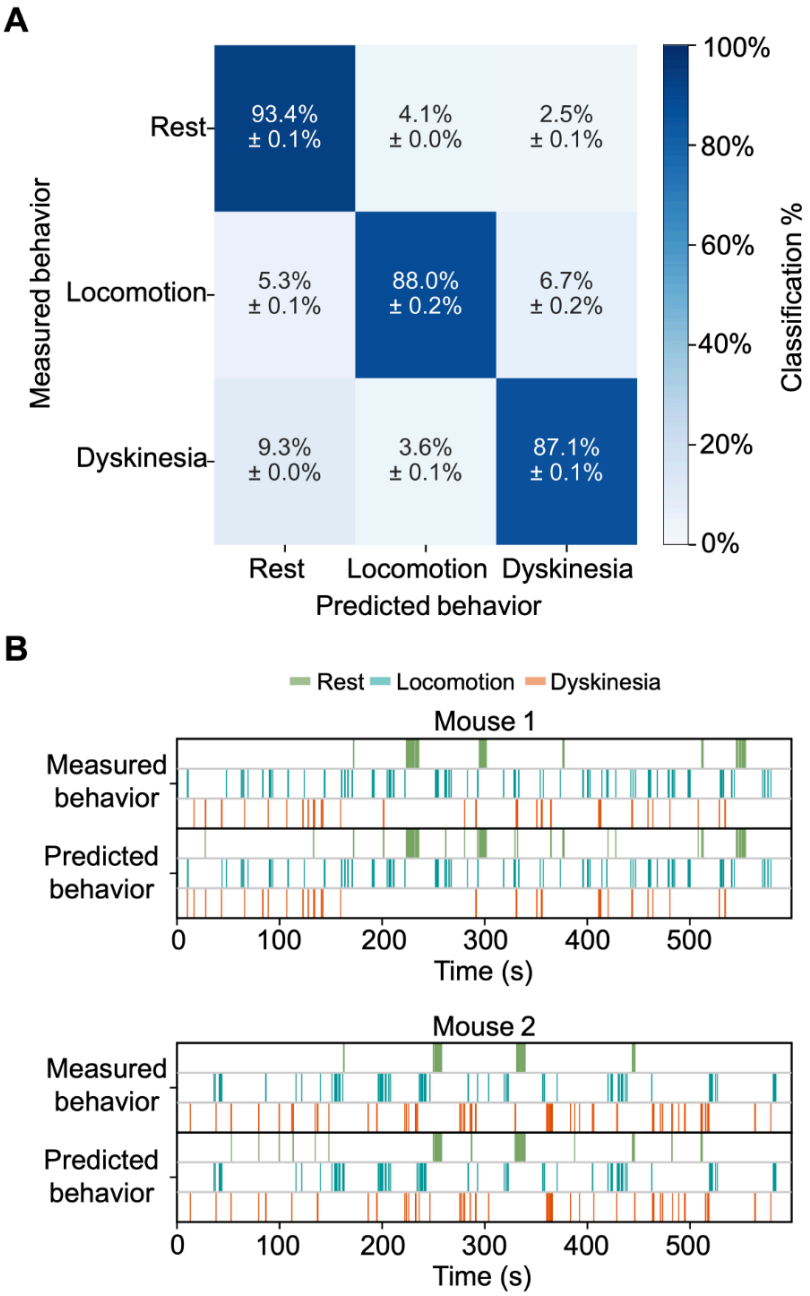

Figure 7. Distinct striatal neural ensemble activity patterns encode locomotion and dyskinesia.

(A) Confusion matrix summarizing behavioral state classification performance across all mice and imaging planes using SVM decoders (**Methods**). Rows indicate empirically determined behavioral states (rest, locomotion, dyskinesia), and columns indicate SVM-predicted states. Each matrix element contains a mean ± s.d correct or incorrect classification accuracy. The confusion matrix was generated by training SVMs across 100 different splits of the data into training and testing subsets and then averaging the results. The high classification accuracy and minimal misclassifications of locomotion and dyskinesia support the notion that these behaviors are represented by distinct neural representations in the dorsolateral striatum. (n = 120 L-DOPA (10 mg/kg) and L-DOPA (10 mg/kg) + amantadine blocks from 6 mice).

(B) Example time series from two experimental blocks and two mice, showing the empirically measured and SVM-predicted behavioral states. Each colored line denotes a segment of time that was classified as rest (green), locomotion (cyan), or dyskinesia (orange). The decoder successfully distinguished between locomotion and dyskinesia with high accuracy (92% and 87% for the blocks shown for mouse 1 and mouse 2, respectively).

Supplemental Figure 1

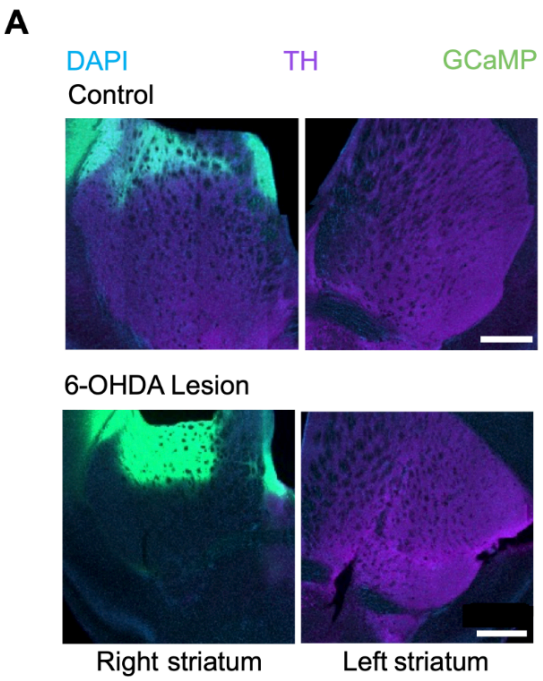

Supplemental Figure 1. Validation of dopamine depletion via fluorescence immunostaining for tyrosine hydroxylase.

(A) We immunostained brain slices for tyrosine hydroxylase to evaluate the loss of dopaminergic axons in the striatum (Purple = Tyrosine Hydroxylase (TH) immunostaining; green = jGCaMP7f; blue = DAPI). *Top*, Images of tissue slices from an example control mouse, showing relatively symmetric tyrosine hydroxylase staining bilaterally. *Bottom*, Images of tissue slices from a mouse with a unilateral 6-OHDA lesion of the SNc, showing loss of dopaminergic axons in the left striatum, ipsilateral to the lesioned SNc. Scale bars: 500 μm.

Supplemental Figure 2

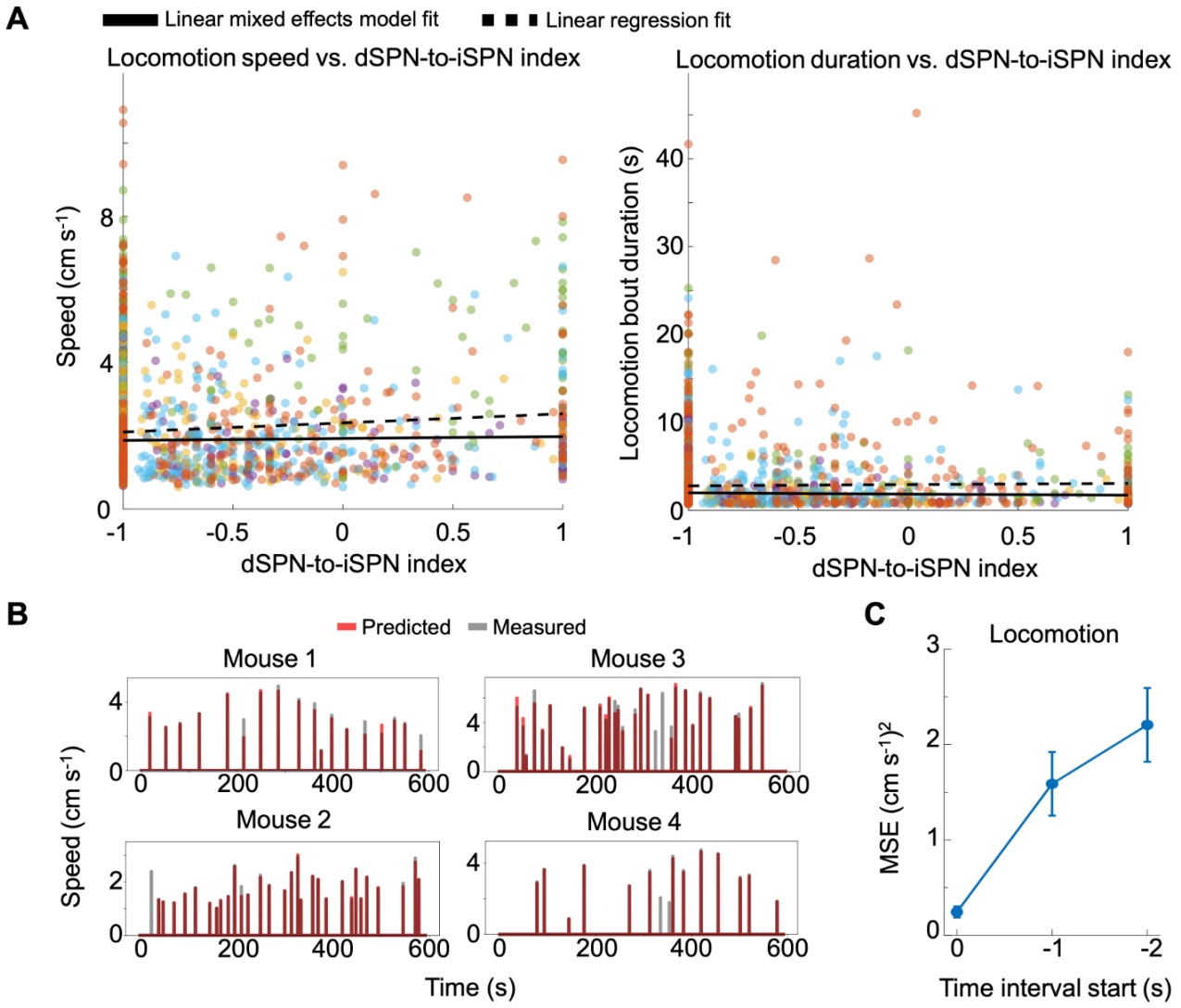

Supplemental Figure 2. Neural ensemble representations, but not the dSPN-to-iSPN index, predict the speed of upcoming locomotion.

(A) Scatter plots showing a lack of association between the dSPN-to-iSPN index during 2-s-long pre-locomotion periods and the speed (*left*) or duration (*right*) of the upcoming locomotion bout. Each data point denotes an individual locomotion bout, with colors denoting individual mice. Data is pooled across 50 pre-lesion, 53 saline, 53 amantadine, and 37 L-DOPA (1 mg/kg) blocks. Solid black lines: Fits from a linear mixed-effects model, in which the systematic variations across mice were treated as random effects and the variations across brain state and treatment conditions were treated as fixed

effects. Dashed black lines: Fits from a least-squares regression applied to the pooled dataset without accounting for condition- or mouse-specific effects. For plots of locomotion speed *vs*. dSPN-to-iSPN index, the mixed-effects model yielded p = 0.3 and the linear regression yielded $R^2 = 0.009$. For plots of locomotion bout duration *vs*. dSPN-to-iSPN index, the mixed-effects model yielded p = 0.3 and the linear regression yielded $R^2 = 0$.

(B) Example time series plots showing predicted (red) and empirically measured (gray) locomotor speeds right after locomotion onset, using the multivariate ridge regression model from **Figure 3A**.

(C) Multivariate ridge regression performance results (**Figure 3A**, **Methods**) across different time intervals of 4-s-duration, shifted progressively further back in time from locomotion onset. The mean squared error (MSE) is plotted as a function of the start time of the 4-s-window, showing how the ability to predict locomotor speed based on neural activity patterns declines with increasing temporal separation from locomotion onset. Error bars: s.e.m. for n = 193 experimental blocks comprising 50 pre-lesion blocks, 53 saline blocks, 53 amantadine blocks, and 37 L-DOPA (1 mg/kg) blocks from 5 mice.

Supplemental Figure 3

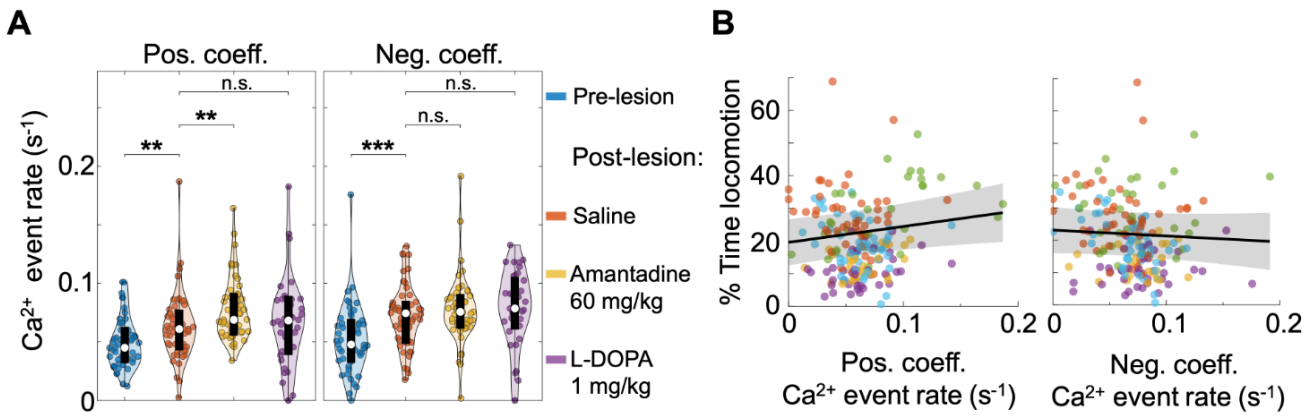

Supplemental Figure 3. The resting activity of positive locomotion-related neurons increases with amantadine treatment and is predictive of the percentage of time spent in locomotion.

(A) Violin plots of mean resting period Ca^{2+} event rates of positive and negative locomotion-related neurons across conditions (**p < 0.01, ***p < 0.001; n.s. = not significant; two-sided rank sum tests corrected for multiple comparisons using a Benjamini–Hochberg procedure with a false-discovery rate of 0.05; n = 50 pre-lesion blocks, 53 saline blocks, 53 amantadine blocks, and 37 L-DOPA (1 mg/kg) blocks from 5 mice).

(B) Linear mixed-effects models show that the mean resting Ca^{2+} event rate of positive locomotor neurons significantly predicts the percentage of time spent ambulating (p = 0.03), whereas the mean resting Ca^{2+} event rate of negative locomotor neurons does not (p = 0.4). Points denote data from individual experimental blocks, color-coded by mouse, with regression lines fit for the untreated hypokinetic (saline control) condition (n = 193 experimental blocks comprising 50 pre-lesion blocks, 53 saline blocks, 53 amantadine blocks, and 37 L-DOPA (1 mg/kg) blocks from 5 mice).

Supplemental Figure 4

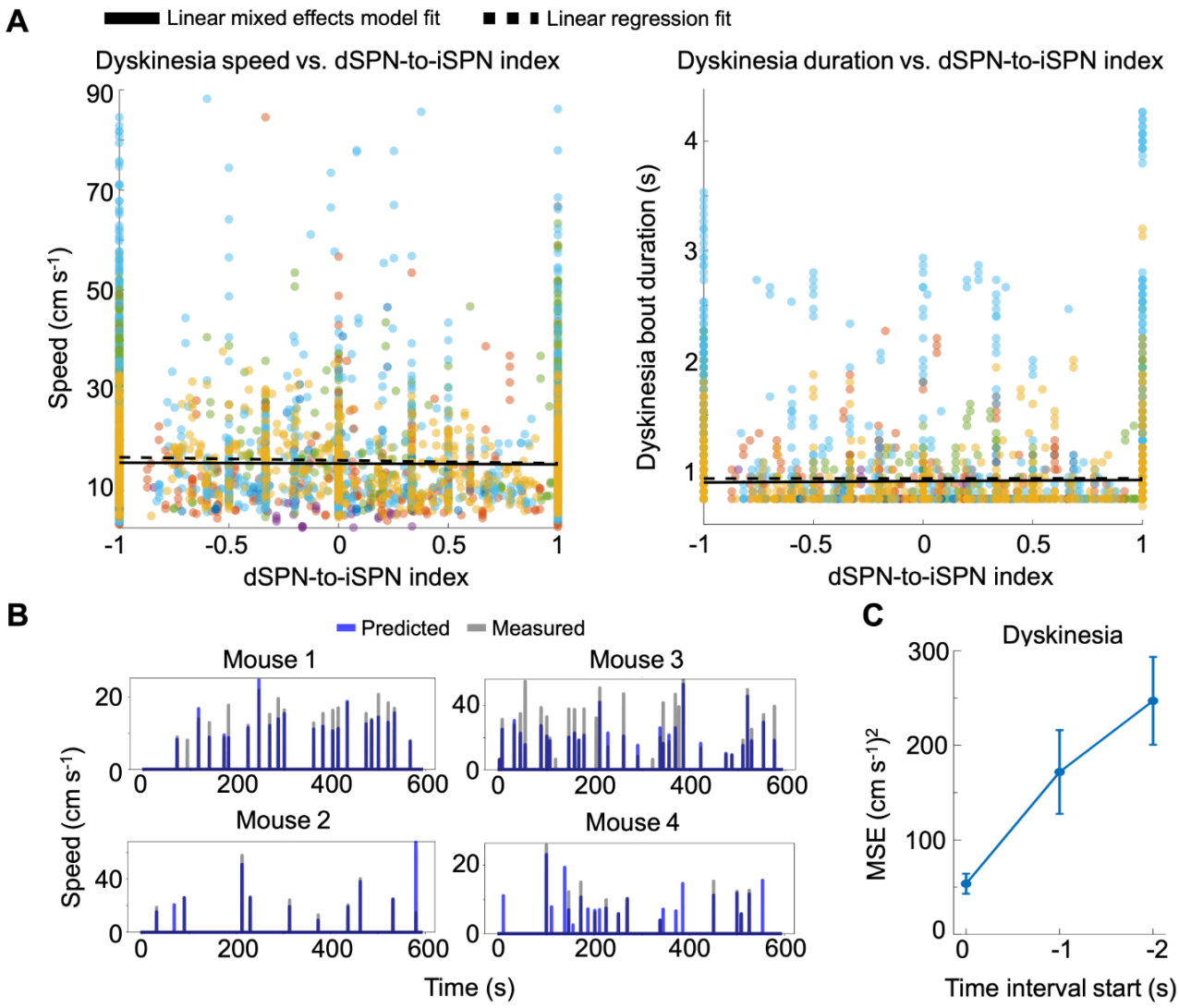

Supplemental Figure 4. Neural ensemble activity patterns, but not the dSPN-to-iSPN index, predicts the kinematic attributes of upcoming dyskinesia bouts.

(A) Scatter plots showing a lack of clear association between pre-dyskinesia dSPN-to-iSPN index values and either the speed (*left*) or duration (*right*) of upcoming dyskinetic movements. Each point denotes data from an individual bout of dyskinesia, with each color denoting an individual mouse. Data is pooled across 57 L-DOPA (10 mg/kg) blocks and 54 L-DOPA (10 mg/kg) + amantadine blocks. Solid black lines: Fits from a linear mixed-effects model, in which the systematic variations across mice were treated as random effects, and the variations across brain state and treatment conditions

were treated as fixed effects. Dashed black lines: Fits from a least-squares regression applied to the pooled dataset without accounting for condition- or mouse-specific effects. For plots of dyskinesia forelimb speed *vs*. dSPN-to-iSPN index, the linear mixed-effects model yielded $p = 0.3$, and the pooled linear regression yielded $R^2 = 0.002$. For plots of dyskinesia duration *vs*. dSPN-to-iSPN index, the linear mixed-effects model yielded $p = 0.06$, and the pooled linear regression yielded $R^2 = 0$.

(B) Example time series plots showing predicted (blue) and empirically measured (gray) forelimb speeds for dyskinetic movements, right after dyskinesia onset. Predicted speeds were based on the multivariate ridge regression model of **Figure 5A**.

(C) Multivariate ridge regression performance results (**Figure 5A**, **Methods**) for different time intervals of 4-s-duration, shifted progressively further back in time from dyskinesia onset. The mean squared error (MSE) is plotted as a function of the start time of the 4-s-window, showing how the ability to predict the speed of dyskinetic forelimb movements based on neural activity patterns declines with increasing temporal separation from dyskinesia onset. Error bars: s.e.m. for n = 111 experimental blocks, comprising 57 L-DOPA (10 mg/kg) blocks and 54 L-DOPA (10 mg/kg) + amantadine blocks from 6 mice.

Supplemental Figure 5

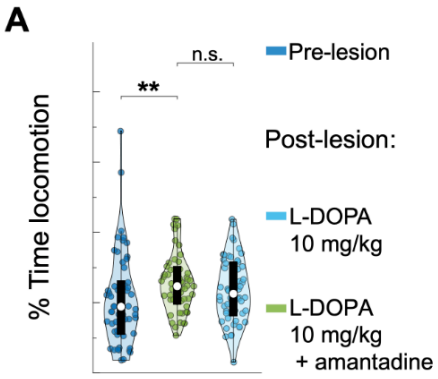

Supplemental Figure 5. The percentage of time that dyskinetic mice spent ambulating was unaffected by amantadine treatment.

(A) Violin plots of the percentage of time spent in locomotion for individual experimental blocks, across 3 different conditions. (**$p < 0.01$; two-sided rank sum tests corrected for multiple comparisons using a Benjamini–Hochberg procedure with a false-discovery rate of 0.05; n = 56 pre-lesion blocks, 57 L-DOPA (10 mg/kg) blocks, 56 L-DOPA (10 mg/kg) + amantadine blocks from 6 mice).

Supplemental Figure 6

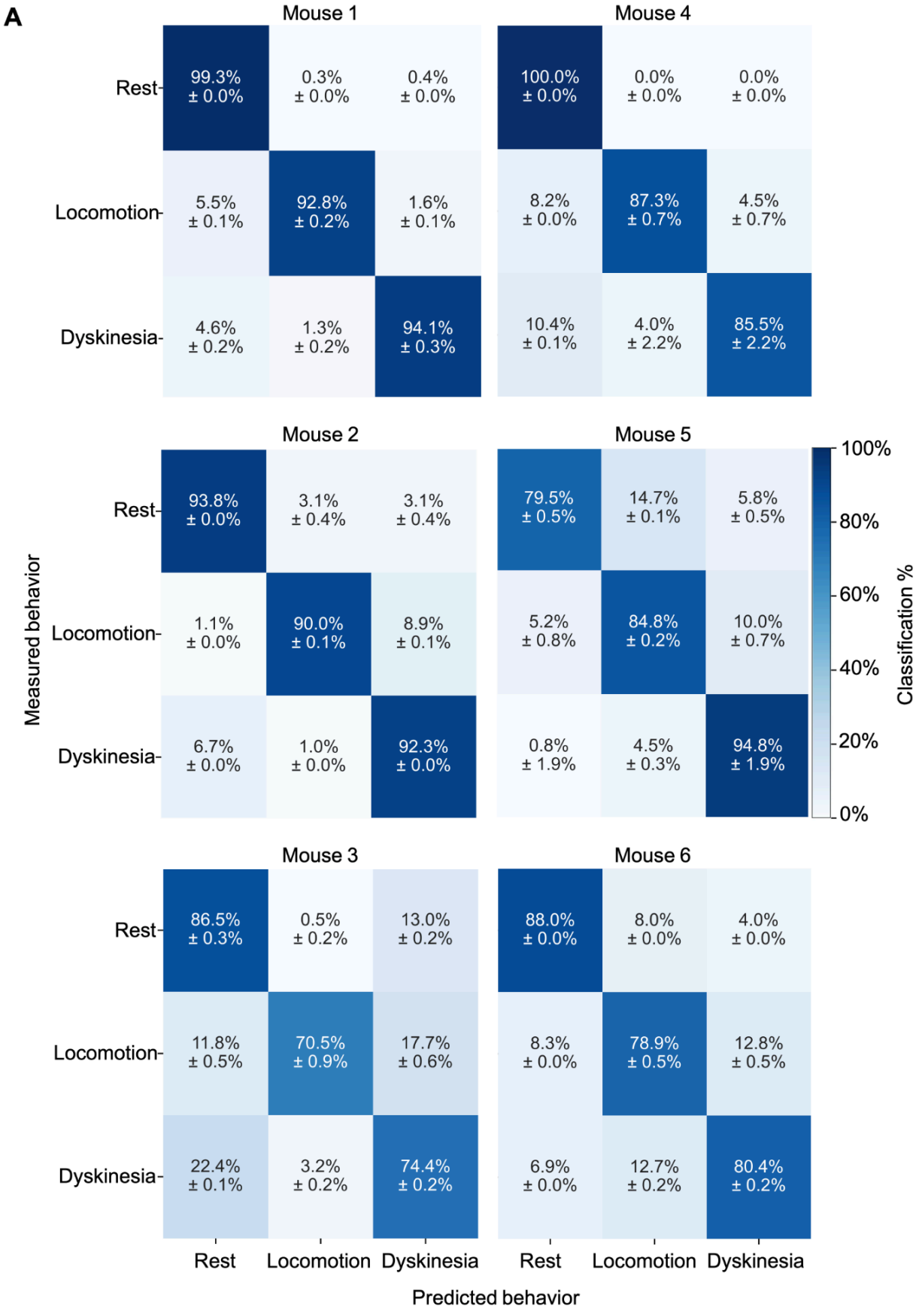

Supplemental Figure 6. SVM decoders of neural ensemble activity can differentiate between periods of locomotion and dyskinesia.

(A) Confusion matrices for individual mice, showing behavioral state classification performances using SVM decoders of neural ensemble activity patterns. Methods and plot format are the same as those for **Figure 7A** (n = 22 blocks for Mouse 1, n = 24 blocks for Mouse 2, n = 16 blocks for Mouse 3, n = 24 blocks for Mouse 4, n = 14 blocks for Mouse 5, and n = 20 blocks for Mouse 6).

Supplemental Figure 7

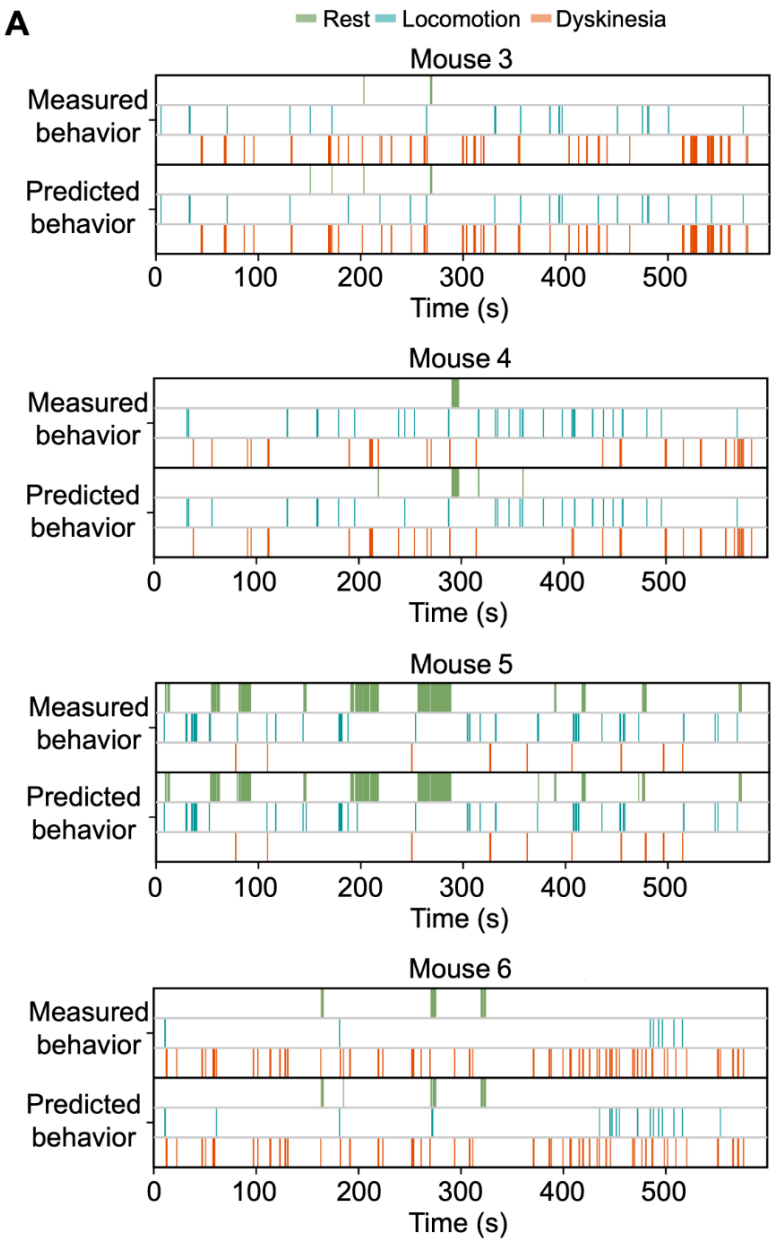

Supplemental Figure 7. Distinct striatal activity patterns encode locomotion and dyskinesia.

(A) Example time series in the same format as those of **Figure 7B**, showing plots of empirically measured and SVM-predicted behavioral states for 4 additional mice.

METHODS

EXPERIMENTAL MODEL AND STUDY PARTICIPANT DETAILS

Viral vectors

We obtained the plasmid, pGP-AAV-syn-jGCaMP7f-WPRE (#104488, Addgene)[24], and subcloned the genetic sequence encoding jGCaMP7f from this plasmid into an AAV backbone with the Camk2a promoter, followed by the WPRE-hGH PolyA sequence, to create the plasmid pAAV-Camk2a-jGCaMP7f-WPRE.hGH. The Viral Tools facility at the HHMI Janelia Research Campus manufactured the virus AAV2/9-Camk2a-jGCaMP7f-WPRE.hGH, which we used at 5E12 GC/µL concentration to express jGCaMP7f in striatal neurons.

Pharmacological agents

In our study, we used the following pharmacological agents:

- 6-Hydroxydopamine hydrobromide (6-OHDA): Obtained from Fisher Scientific (50-194-8364; Purity: ≥99.9%). Solvent: Dissolved in 0.9% saline with 0.02% L-ascorbic acid (A92902, Sigma-Aldrich).
- Levodopa (L-DOPA): Obtained from Sigma-Aldrich (PHR1271; Purity: ≥99.7%). Solvent: Dissolved in 0.9% saline.
- Benserazide hydrochloride: Obtained from Sigma-Aldrich (B7283; Purity: ≥98%). Solvent: Dissolved in 0.9% saline.
- Amantadine hydrochloride: Obtained from Sigma-Aldrich (A1260; Purity: ≥98%). Solvent: Dissolved in 0.9% saline.
- Desipramine hydrochloride: Obtained from Fisher Scientific (30-675-0; Purity: >99%). Solvent: Dissolved in 0.9% saline.

The 0.9% saline solution (Hospira) contained 154 mEq/L of sodium (Na^+) and 154 mEq/L of chloride (Cl^-), with a calculated osmolarity of 308 mOsmol/L. To ensure their stability and efficacy, we prepared all solutions fresh on the day of the experiment.

Mice

The Stanford Administrative Panel on Laboratory Animal Care (APLAC) approved all experiments. To facilitate concurrent recordings and the differentiation of direct pathway spiny projection neurons (dSPNs) and indirect pathway spiny projection neurons (iSPNs), we used a mouse line expressing the red fluorophore tdTomato specifically in dSPNs. We first crossed homozygous Drd1a^{cre} mice[22] with homozygous Ai14 reporter mice (Gt(ROSA)26Sor$^{tm14(CAG-tdTomato)Hze}$; Allen Brain Institute)[23], which express the red fluorophore tdTomato in a Cre-dependent manner, to generate double heterozygous offspring. We intercrossed the double heterozygous mice to produce homozygous Ai14 / homozygous Drd1a^{cre} mice, which then served as breeders for all mice used in the experiments. (We previously used the same type of double transgenic mice in an earlier study.[4]) Here, our data came from 3 female and 3 male mice, aged 16–36 wks at the start of behavioral experiments. We housed mice in 12-h light/dark cycle conditions. We group housed mice (2–5 per cage) before surgery and housed them individually after surgery.

METHOD DETAILS

Surgeries

To enable repeated imaging of striatal neurons and to model a parkinsonian state, we performed the surgeries described below. For all surgeries, we anesthetized mice with isoflurane (1-4% in O_2) and positioned them within our stereotaxic apparatus using ear bars (Model 963, David Kopf instruments).

To express a genetically encoded Ca^{2+} indicator (jGCaMP7f)[24] in SPNs of the dorsolateral striatum (DLS), we performed a stereotaxic injection of 500 nL AAV2/9-CamkII-jGCaMP7f (5E12 GC/μL) into the right DLS (anteroposterior (AP): +0.5 mm from bregma; mediolateral (ML): +2.3 mm from bregma; dorsoventral (DV): -2.3 mm).[18] We performed injections with an UMP3 Ultramicropump (UMP3-3, World Precision Instruments) and NanoFil syringe with a 33-gauge beveled tip (NF33BV, World Precision Instruments). Virus injections were performed at a rate of 200 nL/min. After injections, we sutured the scalp and allowed mice to recover for 1 week.

To allow *in vivo* imaging of SPN activity in the DLS, we removed the scalp and used a 1.4-mm-diameter drill bit to create a craniotomy over the right DLS. Using a 27-gauge needle attached to wall-mounted vacuum tubing, we aspirated the overlying brain tissue and implanted an optical guide tube into the craniotomy site with the end of the tube at a depth of –2.0 mm DV. We created the optical guide tube by gluing a ~1.1 mm diameter disc of 0.1 mm Schott glass (custom fabricated, TLC International) to the tip of a 3.8-mm-long, 18-gauge stainless steel tube (custom fabricated, Ziggy's Tubes and Wires). After the guide tube was in place, we placed a 1-mm-diameter, 4-mm-long gradient index (GRIN) lens (NA 0.5, Pitch 0.5, 1050-004595, Inscopix) into the tube, and we attached a steel headbar to the skull to allow head-fixation. We affixed the full assembly (head bar, optical guide tube with GRIN lens) to the skull by applying first an ultraviolet-light-curing adhesive (Loctite #4305, IDH:303389, R.S. Hughes) and then dental cement (Stoelting Dental Cement, #10000786, Fisher Scientific). We left an open area over the right posterior aspect of the skull (an approximately circular area with a 2-mm-diameter centered on AP: –3.0 mm; ML: +1.3 mm) to facilitate the subsequent injection of 6-OHDA to the substantia nigra pars compacta (SNc).

Mice recovered for 3 weeks after this implantation surgery before starting imaging and behavioral experiments. After completing pre-lesion behavioral and neural recordings, we induced a hemiparkinsonian state by performing a unilateral 6-OHDA lesion to selectively ablate dopaminergic neurons in the SNc. To prevent lesioning of non-dopamine monoamine neurons, we first injected mice with desipramine (25 mg/kg; i.p.; Fisher Scientific) 20 min before 6-OHDA injections. We then stereotaxically injected 6-OHDA (2 µg/µL, dissolved in 0.02% L-ascorbic acid in 0.9% saline; 6-OHDA from Fisher Scientific, L-ascorbic acid from Sigma-Aldrich) in the right SNc (AP: –3.0 mm; ML: +1.3 mm) at 3 depths below the dura (–4.2, –4.0, and –3.8 mm DV; 1.3 µL of 6-OHDA solution at each depth).[4] Mice recovered for at least 2 wks before starting the next round of experiments (post-lesion behavior and neural recordings).

Behavioral recordings

We head-fixed mice and placed them on a custom 3D-printed running wheel (a 4.3-cm-diameter,

10-cm-long cylinder) equipped with a rotary encoder that provided wheel position information. We positioned a camera (DMK37BUX273, The Imaging Source) and infrared illuminator (AI4, Tendelux) in front of the mice to record behavior, such as forelimb movements. A custom hardware and software setup (National Instruments myRIO, Labview 2019) time-locked the neural recordings with the behavioral readouts from the rotary encoder and camera. For each image frame recorded by the two-photon microscope (30 fps), one measurement was recorded from the rotary encoder (making it a 30-Hz-recording) and 3 frames were recorded by the camera, making it a 90-fps-recording. See 'Two-photon Ca^{2+} imaging' below for more details.

Two-photon Ca^{2+} imaging

Once mice were implanted with the optical guide tube and GRIN lens in the dorsolateral striatum (see 'Surgeries'), we acquired Ca^{2+} imaging data from 3 different axial planes (at least 20 μm apart in depth) in the brains of head-fixed mice free to walk or run in place on a wheel. During each imaging session, we imaged the 3 planes sequentially (plane 1, then plane 2, then plane 3) and performed this sequence twice, yielding two recordings per plane. For each session, we positioned head-fixed mice such that the GRIN lens was placed under the objective lens (NA 0.8, CFI75 LWD 16X W, Nikon) of a custom-built two-photon microscope.

We performed two-photon imaging using ultrashort-pulsed laser illumination (940 nm wavelength, to excite both GCaMP and tdTomato) emitted by a wavelength-tunable Ti:sapphire laser (MKS Spectra-Physics, Insight X3, with dispersion compensation). We used two-stage control of the laser illumination power, with an achromatic quarter-wave plate (Thorlabs, AQWP10M-980, 690–1200 nm) and a polarization-dependent beam splitter to provide coarse attenuation, followed by an electro-optical modulator (EOM; Conoptics) to provide fine control and fast blanking. Depending on the specific setup, either a Conoptics EOM 350-80-LA-02 with a 302RM driver or a Conoptics AP214 EOM was used for high-speed modulation and rapid laser blanking during galvanometer turnaround.

Laser beam scanning was performed by two galvanometric mirrors, including a resonant scanner (8 kHz) for the fast scanning axis (Novanta Photonics, formerly Cambridge Technology,

CRS8K 6215H 6SD11015 SYS 2X). Fluorescence emissions were directed onto gated photomultiplier tubes (PMTs; Hamamatsu, H11706P-40 and H10770PA-40 for green and red channels, respectively). The microscope objective lens was a Nikon 16×, NA = 0.8, with a 3 mm working distance (WD). A custom overhead collimated laser diode (532 nm wavelength, Thorlabs, CPS532) was used to check the proper mechanical alignment of the mouse by monitoring the back reflections of the diode laser beam from the sample GRIN. The mouse stood on a custom platform equipped with two goniometers to maintain a fixed orientation. We operated the microscope using a customized version of ScanImage software (version 5.6.1, MBF Biosciences, formerly Vidrio Technologies), which enabled real-time image acquisition (~30 fps, 512 × 512 pixels), hardware control, axial focusing, z-stack collection, and custom metadata saving. Customizations included X-Y sample translation, provided by a motorized Sutter MP-285 stage, and fine axial (Z) control performed by a piezoelectric stage (PI, Q-545.240) with an E-873.1AT controller.

Synchronization of the two-photon microscope (~30 Hz frame acquisition rate) and the faster behavioral camera was achieved using a custom solution based on a National Instruments MyRIO FPGA. The MyRIO detected rising edges of the two-photon frame clock, measuring the interval between consecutive edges to determine the nominal period (T). It generated a train of short (~100 µs) electronic pulses, subdividing T into m equal intervals (typically m=3), and transmitted these pulses through digital I/O lines as frame triggers for the behavioral camera. The clock upsampling yielded a simple relationship between the number of two-photon image frames (n) and the total frames acquired by the behavioral camera ((n-1)×m). Each frame from the behavioral camera was time-locked to the two-photon image sequence, eliminating a need for offline resampling or temporal alignment. Real-time communication between the MyRIO and the microscope software was managed via built-in LabVIEW interfaces and FIFO communication. Trigger signals and timestamps were logged in comma-separated files provided by a PC host computer operating the MyRIO.

Drug treatments

To assess the effects of different pharmacological interventions on motor behavior and neuronal activity in the parkinsonian state, 2–8 wks after the 6-OHDA lesion we began post-lesion experimental sessions. 20 min before each set of 'post-lesion' session, we injected mice with either: 0.9% saline (post-lesion control), amantadine (60 mg/kg), L-DOPA (1 mg/kg) + benserazide (15 mg/kg), L-DOPA (10 mg/kg) + benserazide (15 mg/kg), or L-DOPA (10 mg/kg) + benserazide (15 mg/kg) + amantadine (60 mg/kg) (amantadine, L-DOPA, and benserazide all from Sigma-Aldrich). (In all sessions that we administered L-DOPA, we co-administered benserazide to prevent peripheral conversion of L-DOPA to dopamine). We selected doses based on prior studies.[4,30] We dissolved all compounds in 0.9% saline and delivered them intraperitoneally (i.p.) with a 30 mL/kg injection volume. We performed drug treatment sessions 1–10 d apart. We found in exploratory studies that the ordering of drug treatments was very important, as injections of L-DOPA would prime the mice for dyskinesias, and mice could then have dyskinesias even without L-DOPA injections. Therefore, saline-only sessions were always done first, then amantadine only sessions, and then L-DOPA (1 mg/kg) sessions. Finally, we alternated L-DOPA (10 mg/kg) and L-DOPA (10 mg/kg) + amantadine sessions, with the first session of L-DOPA (10 mg/kg) always occurring before the first L-DOPA (10 mg/kg) + amantadine session (**Figure 1E**). During each session, there were 6 blocks of two-photon imaging and behavioral recording, each 10 min in duration, corresponding to two sequential passes through 3 different axial planes in the DLS.

Immunohistochemistry

After the completion of imaging experiments, we euthanized and intracardially perfused the mice with phosphate-buffered saline (PBS) (Gibco) and then a 4% solution of paraformaldehyde (Electron Microscopy Sciences) in PBS. We sliced the fixed brain tissue using a vibratome (VT1000s, Leica) to obtain 80-µm-thick coronal sections. We immunostained the tissue sections with polyclonal antibodies against tyrosine hydroxylase (TYH 1:500, Aves Labs) and applied the secondary antibody Alexa Fluor 647 goat anti-chicken IgG(H+L) (A-21449, Thermo Fisher). We visualized immunofluorescence in our

sections using a slide-scanning microscope (Axio Imager Z1, Zeiss) and confirmed that all mice included for analyses had a complete unilateral loss of dopaminergic signal in the striatum and substantia nigra pars compacta (SNc) (**Supplemental Figure 1A**).

QUANTIFICATION AND STATISTICAL ANALYSIS

Behavioral analyses

We performed automatic limb position tracking from the behavioral video recordings using DeepLabCut (version 2.0).[28] We classified locomotion periods as intervals when the speed of the wheel was > 0.5 cm/s. We classified dyskinesia periods as intervals when the left forelimb, contralateral to the 6-OHDA lesion in all mice, was moving at an average speed > 2.5 cm/s (with at least 3 frames during the period reaching > 30 cm/s) and when there was no sign of locomotion on the running wheel (**Figures 1E,C**). For behavioral analyses, we defined the following types of periods: **pre-locomotion**, a 2-s-period preceding locomotion onset; **pre-dyskinesia**, a 2-s-period preceding dyskinesia onset; and **rest**, periods of inactivity at least 1 s after locomotion or dyskinesia offset and at least 1 s before locomotion or dyskinesia onset. To analyze the resting activity of locomotion- and dyskinesia-related neurons, we excluded rest periods that occurred within 4 s of locomotion or dyskinesia onset. This ensured that data intervals used in multivariate regression analyses for the identification of neural activity patterns related to upcoming locomotion or dyskinesia were not reused in the subsequent analyses of the resting activity of these same neurons.

Analysis of Ca^{2+} video datasets

We pre-processed Ca^{2+} videos by temporally downsampling each movie twofold and then corrected computationally for rigid and non-rigid lateral motion of the brain using the NoRMCorre image registration routine.[39] To obtain activity traces of individual neurons' relative changes in [Ca^{2+}]-related fluorescence ($\Delta F(t)/F$) from the motion-corrected Ca^{2+} videos, we used the cell extraction routine EXTRACT.[40,41] From each neuron's extracted Ca^{2+} activity trace, we identified Ca^{2+} transient events via detection of fluorescence peaks that were ≥ 2 s.d. above the cell's mean baseline fluorescence level and lasted for ≥ 0.2 s. We determined the time of each Ca^{2+} event as the temporal midpoint

between the time of the Ca^{2+} event's fluorescence peak and the most recent preceding trough in fluorescence. To classify neurons found by EXTRACT as either dSPNs or iSPNs, we first used the software Cellpose to determine the outlines of all cells expressing tdTomato.[42,43] Each neuron determined by EXTRACT to have a spatial profile within the outline of a tdTomato-expressing-cell was classified as a dSPN. We classified all other neurons found by EXTRACT as iSPNs.

Identification of behavior-related neurons

To identify striatal neurons with activation patterns related to either voluntary locomotion or involuntary dyskinesias, we performed linear regression analyses to identify SPNs the activity of which predicted the mouse's upcoming movement speed.

To do this, we built predictive models that linked neural activity to the speed of either locomotion or dyskinetic forelimb movements (**Figures 3A, 5A**; **Supplemental Figures 2B, 4B**). For each behavioral block, we first identified the onset time of each locomotion or dyskinesia bout and measured the initial movement speed over the first 0.66 s following movement onset. This value served as the behavioral response variable. We also included 10 periods of inactivity (*i.e.*, when neither locomotion nor dyskinesia occurred) as additional response variables in the dataset.

For each behavioral onset, we used SPN activity from the interval [–4 s, 0 s] just prior to movement onset to create a predictor matrix. Each row in this matrix corresponded to a single movement or rest period. Each column of the matrix contained the mean Ca^{2+} event rates of an individual neuron across the set of pre-movement periods. This approach allowed us to examine how neural activity prior to movement related to the upcoming behavioral outcome.

To account for differences in the scale and distribution of neural activity, we z-scored all predictor variables and applied a log-transformation to the response variable to mitigate skewness. We then used a ridge regression model (**cuml.linear_model.Ridge** module, RAPIDS AI framework) to predict the speed of locomotion or dyskinesia forelimb movements based on the neural activity patterns. We chose ridge regression for its capability to handle multicollinearity between neurons and a use of L_2 regularization. We trained the regression model separately for each dataset using a

regularization parameter (alpha) of 1.0, and we evaluated its performance based on its mean squared error (MSE) and the coefficient of determination (R^2) on the training dataset.

To identify behavior-related neurons, we examined the coefficients determined for each neuron in the ridge regression models. We classified neurons with strong positive regression coefficients (z-score > +1 above those of the mean across all neurons) in the locomotion models as positive locomotion-related neurons and those with strong negative coefficients (z-score < –1) as negative locomotion-related neurons. Similarly, we classified neurons with strong positive coefficients (z-score > +1) in the dyskinesia models as positive dyskinesia-related neurons. We validated the behavioral associations of these neuron classes by comparing the speeds of locomotion or forelimb movement in the interval [0 s, 0.66 s] prior to Ca^{2+} event onset to those in the interval [3.33 s, 4 s] after onset. We separately performed regression analyses for identifying positive locomotion- and positive dyskinesia-related neurons, implying that, in principle, individual neurons could be classified as both, even though few were (**Figure 6D**).

Our main analyses focused on the [–4 s, 0 s] interval just prior to movement. However, to test the extent to which neural signals predictive of movement arose before movement onset, we conducted ancillary analyses in which we progressively shifted the predictor window backwards in time from movement onset (**Supplemental Figures 2C**, **4C**). As expected, predictive performances declined as the prediction window moved further in time from the moment of movement onset.

We constructed regression models separately for each mouse, drug condition, and optical plane. For each of these datasets, we included the two recording blocks performed at each optical plane, and we tracked individual neurons across blocks whenever possible based on spatial alignment. Not all neurons were present in every block, which could in principle bias the determinations of regression coefficients. However, the z-scored regression coefficients for each neuron did not meaningfully correlate with the number of blocks in which the neuron was detected, suggesting that coefficient strength was not simply driven by the number of blocks in which we recorded a cell's activity. This approach allowed us to include more behavioral bouts per neuron, with the aim of improving the accuracy with which the regression coefficients could be determined.

Index measures of SPN activity

To quantify the relative levels of dSPN and iSPN activity, we computed a dSPN-to-iSPN index, defined as the difference between the mean Ca^{2+} event rates for dSPNs ($Rate_{dSPN}$) and iSPNs ($Rate_{iSPN}$), divided by their sum: $(Rate_{dSPN} - Rate_{iSPN})/(Rate_{dSPN} + Rate_{iSPN})$.

To quantify the relative activity levels of positive and negative locomotion-related neurons, we calculated a 'locomotor neuron index, defined as the difference between the mean Ca^{2+} event rates for positive ($Rate_{Positive\_Locomotion}$) and negative locomotion-related neurons ($Rate_{Negative\_Locomotion}$), divided by their sum:

$$(Rate_{Positive\_Locomotion} - Rate_{Negative\_Locomotion})/(Rate_{Positive\_Locomotion} + Rate_{Negative\_Locomotion}).$$

We calculated an analogous index for positive dyskinesia- and positive locomotion-related cells (a 'dyskinesia-to-locomotion positive coefficient index').

Linear mixed-effects model

To analyze whether the resting state activity levels of specific neurons were predictive of the extent of mouse movement, we applied linear mixed-effects models across multiple brain states, treatment conditions and individual mice (**Figures 3F, 5F**). In these models, we included the neural activity metric of interest (*e.g.*, dSPN-to-iSPN index, locomotor neuron index, or positive dyskinesia-related neuron mean Ca^{2+} event rate) as a continuous fixed effect, the experimental condition as a categorical fixed effect, and mouse identity as a random effect that accounted for inter-mouse variability. For locomotion and dyskinesia behaviors, we specified the models as:

$$Y_{ij} = \beta_0 + \beta_1 X_{ij} + \beta_2 C_{ij} + u_i + \varepsilon_{ij}$$

where:

Y_{ij} = Percentage of time spent in locomotion or dyskinesia for mouse i in block j

X_{ij} = Neural activity metric (*e.g.*, dSPN-to-iSPN index) for mouse i in block j

C_{ij}= Condition (categorical fixed effect)

u_i= Random intercept for mouse i

ε_{ij}= Residual error

We fit the models using MATLAB's (R2023a, MathWorks) linear mixed-effects modeling framework (**fitlme**) and optimized the parameter estimates by maximum likelihood estimation. We chose an additive model to address whether a general relationship exists between neural activity and behavior across treatment conditions and assessed this relationship by evaluating the estimated slopes and associated p-values from the models.

In addition, we used further linear mixed-effects analyses (**Supplementary Figures 2A, 4A**) to determine, at the level of individual movement bouts, whether the dSPN-to-iSPN index during the pre-movement period was predictive of the kinematic attributes of the upcoming locomotion or dyskinesia bouts. Specifically, we tested whether the dSPN-to-iSPN index in the seconds before movement onset correlated with the speed or duration of the ensuing movement bout. These linear mixed-effects models were constructed similarly as those described above, with the pre-movement dSPN-to-iSPN index used as the neural activity metric (X) and the upcoming locomotion or dyskinesia speed or duration as the outcome variable (Y).

Behavioral state decoding using support vector machines (SVMs)

To determine whether distinct behavioral states—rest, locomotion, and dyskinesia—are separably represented in the dorsolateral striatum (DLS), we trained support vector machine (SVM) decoders to classify behavioral states based on neural activity (**cuml.svm.SVC** module, RAPIDS AI framework). This process involved extracting neural activity features, labeling behavioral states, training the model, and evaluating its performance.

To link neural activity with specific behaviors, we first segmented each experimental block into overlapping 1-s-long time windows. We assigned a behavioral label (rest, locomotion, or dyskinesia) to each window based on the movement measurements during that time period. A time window was classified as one containing locomotion if it ended with at least 0.66 s of continuous locomotion

(without simultaneously detected dyskinesias). A time window was classified as one containing dyskinesia if it ended with at least 0.66 s of dyskinetic movements (see **Behavior** for dyskinesia identification details). To exclude periods with potential transitions between behavioral states, a window was classified as a rest period if neither locomotion nor dyskinesia occurred during the window itself or within 15-s buffer periods before and afterward. Time windows that did not meet any of the above criteria were not included in the datasets used to train or test the SVM decoders.

For each neuron, we represented its activity within a given time window using the cell's mean Ca^{2+} event rate. This yielded a feature vector, in which each element denoted an individual neuron's net activity within the time window. We randomly split the entire dataset, with 80% of time windows used to train the SVM and the remaining 20% used to test it. To balance the class distributions, we applied random oversampling to the training dataset. To assess classification performance while accounting for variability across the train-test splits, we repeated model training and testing 100 times per imaging plane and mouse. In each iteration, we trained a linear support vector classifier on the oversampled training data and evaluated its performance on the held-out test dataset. We then averaged the results across all 100 train-test splits and quantified classification performance by using confusion matrices to compare the sets of measured and predicted behavioral labels (**Figure 7A, Supplemental Figure 6A**). To illustrate classification performance, we generated example decoded time series and plotted the empirically determined mouse behavioral epochs alongside those predicted by the SVM for individual experimental blocks (**Figure 7B, Supplemental Figure 7A**).

Statistical analysis

For two-sample comparisons of a single variable, we used a non-parametric test, either the Wilcoxon rank sum or the Wilcoxon signed-rank test (MATLAB functions, **ranksum** and **signrank**). All tests were two-tailed unless stated otherwise. Where applicable, we corrected for multiple comparisons using a Benjamini–Hochberg procedure with a false-discovery rate of 0.05. To determine statistical significance in the linear mixed-effects models, we used the p-value estimated by the model.

For our violin plots, the shape of the violin illustrates the kernel density estimate (KDE), providing a smoothed representation of the data distribution. This KDE was calculated using MATLAB's default **ksdensity** function, which uses a Gaussian kernel to estimate the probability density function of the data. See also the caption of **Figure 1** for further details about the plot format.

For barplots (**Figures 2D, 4D**), each bin's transition probability was calculated as $p = \frac{x}{y}$ where x is the number of transition trials and y is the total trials in that bin. The probabilities are plotted as percents ($p \times 100$). Error bars indicate the s.e.m. of this proportion, determined as $SE = 100 \times \sqrt{\frac{p(1-p)}{y}}$.

Software

We used ScanImage software (version 5.6.1, MBF Biosciences, formerly Vidrio Technologies) and custom Labview 2019 software (National Instruments) to record two-photon Ca^{2+} videos. We used NoRMCorre for image registration of the Ca^{2+} video frames and EXTRACT for identifying neurons in these videos and determining their fluorescence activity traces.[39–41] We used Cellpose to automatically identify tdTomato expressing neurons.[42,43] We used DeepLabCut (version 2.0) for automatic behavioral tracking.[28]

We performed downstream analyses using custom-written code in MATLAB and Python, using several add-on Python libraries for statistical modeling, machine learning, and data visualization. For behavioral state classification, we implemented support vector machine (SVM) decoders using the **cuml.svm.SVC** module from the RAPIDS AI framework, which provides GPU-accelerated machine learning capabilities. We evaluated classification performance using **scikit-learn's** accuracy_score and confusion_matrix functions. For regression-based analyses, we used **cuml.linear_model.Ridge** for ridge regression, enabling efficient regularized regression modeling. Data preprocessing included z-score normalization, implemented using **StandardScaler** from **scikit-learn**. To manage large datasets, we used **NumPy** for array operations and **pandas** for structured data manipulation. We visualized results using MATLAB, **matplotlib** and **seaborn**, generating heatmaps, scatter plots, and violin plots to characterize classification performances, regression results, and neural activity

distributions. To apply Benjamini-Hochberg corrections for multiple comparisons, we used the MATLAB script **fdr_bh** (*https://www.mathworks.com/matlabcentral/fileexchange/27418-fdr_bh, MATLAB File Exchange*). To create violin plots, we used the code: *Bechtold, Bastian, 2016. Violin Plots for Matlab, Github Project. https://github.com/bastibe/Violinplot-Matlab, DOI: 10.5281/zenodo.4559847*.

REFERENCES

1. DeLong, M.R. (1990). Primate models of movement disorders of basal ganglia origin. Trends Neurosci. *13*, 281–285.
2. Albin, R.L., Young, A.B., and Penney, J.B. (1989). The functional anatomy of basal ganglia disorders. Trends Neurosci. *12*, 366–375.
3. Stoessl, A.J., and Mckeown, M.J. (2016). Movement disorders. Handb. Clin. Neurol. *136*, 957–969.
4. Parker, J.G., Marshall, J.D., Ahanonu, B., Wu, Y.-W., Kim, T.H., Grewe, B.F., Zhang, Y., Li, J.Z., Ding, J.B., Ehlers, M.D., et al. (2018). Diametric neural ensemble dynamics in parkinsonian and dyskinetic states. Nature *557*, 177–182.
5. Girasole, A.E., Lum, M.Y., Nathaniel, D., Bair-Marshall, C.J., Guenthner, C.J., Luo, L., Kreitzer, A.C., and Nelson, A.B. (2018). A Subpopulation of Striatal Neurons Mediates Levodopa-Induced Dyskinesia. Neuron *97*, 787–795.e6.
6. Nelson, A.B., Girasole, A.E., Lee, H.-Y., Ptáček, L.J., and Kreitzer, A.C. (2022). Striatal Indirect Pathway Dysfunction Underlies Motor Deficits in a Mouse Model of Paroxysmal Dyskinesia. J. Neurosci. *42*, 2835–2848.
7. McGregor, M.M., and Nelson, A.B. (2019). Circuit Mechanisms of Parkinson's Disease. Neuron *101*, 1042–1056.
8. Kravitz, A.V., Freeze, B.S., Parker, P.R.L., Kay, K., Thwin, M.T., Deisseroth, K., and Kreitzer, A.C. (2010). Regulation of parkinsonian motor behaviours by optogenetic control of basal ganglia circuitry. Preprint, https://doi.org/10.1038/nature09159 https://doi.org/10.1038/nature09159.
9. Ryan, M.B., Bair-Marshall, C., and Nelson, A.B. (2018). Aberrant Striatal Activity in Parkinsonism and Levodopa-Induced Dyskinesia. Cell Rep. *23*, 3438–3446.e5.
10. Alcacer, C., Andreoli, L., Sebastianutto, I., Jakobsson, J., Fieblinger, T., and Cenci, M.A. (2017). Chemogenetic stimulation of striatal projection neurons modulates responses to Parkinson's disease therapy. J. Clin. Invest. *127*, 720–734.
11. Jankovic, J. (2009). Treatment of hyperkinetic movement disorders. Lancet Neurol. *8*, 844–856.
12. Armstrong, M.J., and Okun, M.S. (2020). Diagnosis and Treatment of Parkinson Disease: A Review. JAMA *323*, 548–560.
13. Singer, C. (2002). Adverse effects in the treatment of Parkinson's disease. Expert Rev. Neurother. *2*, 105–118.
14. Danysz, W., Dekundy, A., Scheschonka, A., and Riederer, P. (2021). Amantadine: reappraisal of the timeless diamond—target updates and novel therapeutic potentials. J. Neural Transm. *128*, 127–169.
15. Cui, G., Jun, S.B., Jin, X., Pham, M.D., Vogel, S.S., Lovinger, D.M., and Costa, R.M. (2013). Concurrent activation of striatal direct and indirect pathways during action initiation. Nature *494*, 238–242.
16. Tecuapetla, F., Jin, X., Lima, S.Q., and Costa, R.M. (2016). Complementary contributions of striatal projection pathways to action initiation and execution. Cell *166*, 703–715.
17. Tecuapetla, F., Matias, S., Dugue, G.P., Mainen, Z.F., and Costa, R.M. (2014). Balanced activity in basal ganglia projection pathways is critical for contraversive movements. Nat. Commun. *5*, 4315.
18. Klaus, A., Martins, G.J., Paixao, V.B., Zhou, P., Paninski, L., and Costa, R.M. (2017). The Spatiotemporal Organization

of the Striatum Encodes Action Space. Neuron *96*, 949.

19. Shen, W., Ren, W., Zhai, S., Yang, B., Vanoye, C.G., Mitra, A., George, A.L., Jr, and Surmeier, D.J. (2020). Striatal Kir2 K+ channel inhibition mediates the antidyskinetic effects of amantadine. J. Clin. Invest. *130*, 2593–2601.

20. Metman, L., Del Dotto, P., van den Munckhof, P., Fang, J., Mouradian, M., and Chase, T. (1998). Amantadine as treatment for dyskinesias and motor fluctuations in Parkinson's disease. Neurology *50*, 1323–1326.

21. Caroff, S.N., Jain, R., and Morley, J.F. (2020). Revisiting amantadine as a treatment for drug-induced movement disorders. Ann. Clin. Psychiatry *32*, 198–208.

22. Lemberger, T., Parlato, R., Dassesse, D., Westphal, M., Casanova, E., Turiault, M., Tronche, F., Schiffmann, S.N., and Schütz, G. (2007). Expression of Cre recombinase in dopaminoceptive neurons. BMC Neurosci. *8*, 4.

23. Madisen, L., Zwingman, T.A., Sunkin, S.M., Oh, S.W., Zariwala, H.A., Gu, H., Ng, L.L., Palmiter, R.D., Hawrylycz, M.J., Jones, A.R., et al. (2010). A robust and high-throughput Cre reporting and characterization system for the whole mouse brain. Nat. Neurosci. *13*, 133–140.

24. Dana, H., Sun, Y., Mohar, B., Hulse, B.K., Kerlin, A.M., Hasseman, J.P., Tsegaye, G., Tsang, A., Wong, A., Patel, R., et al. (2019). High-performance calcium sensors for imaging activity in neuronal populations and microcompartments. Nat. Methods *16*, 649–657.

25. Weglage, M., Wärnberg, E., Lazaridis, I., Calvigioni, D., Tzortzi, O., and Meletis, K. (2021). Complete representation of action space and value in all dorsal striatal pathways. Cell Rep. *36*, 109437.

26. Smith, A.C.W., Jonkman, S., Difeliceantonio, A.G., O'Connor, R.M., Ghoshal, S., Romano, M.F., Everitt, B.J., and Kenny, P.J. (2021). Opposing roles for striatonigral and striatopallidal neurons in dorsolateral striatum in consolidating new instrumental actions. Nat. Commun. *12*, 5121.

27. Jung, J.C., Mehta, A.D., Aksay, E., Stepnoski, R., and Schnitzer, M.J. (2004). In vivo mammalian brain imaging using one- and two-photon fluorescence microendoscopy. J. Neurophysiol. *92*, 3121–3133.

28. Mathis, A., Mamidanna, P., Cury, K.M., Abe, T., Murthy, V.N., Mathis, M.W., and Bethge, M. (2018). DeepLabCut: markerless pose estimation of user-defined body parts with deep learning. Nat. Neurosci. *21*, 1281–1289.

29. Thiele, S.L., Warre, R., and Nash, J.E. (2012). Development of a unilaterally-lesioned 6-OHDA mouse model of Parkinson's disease. J. Vis. Exp. https://doi.org/10.3791/3234.

30. Paquette, M.A., Martinez, A.A., Macheda, T., Meshul, C.K., Johnson, S.W., Berger, S.P., and Giuffrida, A. (2012). Anti-dyskinetic mechanisms of amantadine and dextromethorphan in the 6-OHDA rat model of Parkinson's disease: role of NMDA vs. 5-HT1A receptors. Eur. J. Neurosci. *36*, 3224–3234.

31. Pan, W.X., Mao, T., and Dudman, J.T. (2010). Inputs to the dorsal striatum of the mouse reflect the parallel circuit architecture of the forebrain. Front. Neuroanat. *4*, 147.

32. Alcacer, C., Klaus, A., Mendonça, M., Abalde, S.F., Cenci, M.A., and Costa, R.M. (2024). Abnormal hyperactivity of specific striatal ensembles encodes distinct dyskinetic behaviors revealed by high-resolution clustering. bioRxivorg. https://doi.org/10.1101/2024.09.06.611664.

33. Blanpied, T.A., Clarke, R.J., and Johnson, J.W. (2005). Amantadine inhibits NMDA receptors by accelerating channel closure during channel block. J. Neurosci. *25*, 3312–3322.

34. Shen, W., Flajolet, M., Greengard, P., and Surmeier, D.J. (2008). Dichotomous dopaminergic control of striatal synaptic plasticity. Science *321*, 848–851.

35. Cenci, M.A., and Konradi, C. (2010). Maladaptive striatal plasticity in L-DOPA-induced dyskinesia. Prog. Brain Res. *183*, 209–233.

36. Shen, W., Zhai, S., and Surmeier, D.J. (2022). Striatal synaptic adaptations in Parkinson's disease. Neurobiol. Dis. *167*, 105686.

37. López de Maturana, R., and Sánchez-Pernaute, R. (2010). Regulation of corticostriatal synaptic plasticity by G protein-coupled receptors. CNS Neurol. Disord. Drug Targets *9*, 601–615.

38. Heifetz, A., Southey, M., Morao, I., Townsend-Nicholson, A., and Bodkin, M.J. (2018). Computational Methods Used in Hit-to-Lead and Lead Optimization Stages of Structure-Based Drug Discovery. Methods Mol. Biol. *1705*, 375–394.

39. Pnevmatikakis, E.A., and Giovannucci, A. (2017). NoRMCorre: An online algorithm for piecewise rigid motion correction

of calcium imaging data. J. Neurosci. Methods *291*, 83–94.

40. Dinc, F., Inan, H., Hernandez, O., Schmuckermair, C., Hazon, O., Tasci, T., Ahanonu, B.O., Zhang, Y., Lecoq, J., Haziza, S., et al. (2021). Fast, scalable, and statistically robust cell extraction from large-scale neural calcium imaging datasets. bioRxiv. https://doi.org/10.1101/2021.03.24.436279.

41. Inan, H., Erdogdu, M.A., and Schnitzer, M. (2017). Robust Estimation of Neural Signals in Calcium Imaging. In Advances in Neural Information Processing Systems, I. Guyon, U. V. Luxburg, S. Bengio, H. Wallach, R. Fergus, S. Vishwanathan, and R. Garnett, eds. (Curran Associates, Inc.).

42. Stringer, C., Wang, T., Michaelos, M., and Pachitariu, M. (2021). Cellpose: a generalist algorithm for cellular segmentation. Nat. Methods *18*, 100–106.

43. Pachitariu, M., and Stringer, C. (2022). Cellpose 2.0: how to train your own model. Nat. Methods *19*, 1634–1641.